



SCUOLA DOTTORALE IN INGEGNERIA MECCANICA

SEZIONE DI INGEGNERIA MECCANICA E INDUSTRIALE

XXVIII CICLO

Development of reduced order models for real-time helicopter flight simulation

Dottorando: **Riccardo Gori**

firma

Docente guida: **Prof. Massimo Gennaretti**

firma

Coordinatore: **Prof. Edoardo Bemporad**

firma

Contents

1. Introduction	7
2. State-space main rotor aeroelastic models	9
2.1. State of the art	9
2.2. Finite-state models description	10
2.2.1. Linear time invariant aeroelastic model	11
2.2.2. Linear time periodic aeroelastic model	13
2.2.3. Full flight envelope model	14
2.3. High fidelity models description	16
3. Linear time invariant model extraction from high-fidelity solvers	18
3.1. Linear time invariant transfer function extraction	19
3.1.1. Single frequency excitation method	19
3.1.2. Chirp excitation method	22
3.2. Rational matrix approximation	25
3.2.1. Parametrization of the state-space matrices	26
3.2.2. Nonlinear separable least square	32
3.2.3. Static derivatives imposition	35
3.3. Numerical results	36
3.3.1. Transfer function identification	36
3.3.2. Time-response analysis	39
3.3.3. Influence of the additional states dynamics	42
4. Linear time periodic model extraction from high-fidelity solvers	46
4.1. Introduction to harmonic transfer function	46
4.2. Linear time periodic transfer function extraction	50
4.2.1. Extension of the chirp excitation method to LTP systems	51

Contents

4.3. Numerical results	53
4.3.1. Aerodynamic model	53
4.3.2. Aeroelastic model	57
5. Model stitching	58
5.1. Application of the stitched model in the time domain . . .	60
5.2. Numerical results	62
5.2.1. Validation of the identification process	62
5.2.2. Application to maneuvering flight	64
6. Simulation results	67
6.1. Simulations summary	68
6.1.1. Lateral step input	70
6.1.2. Longitudinal step input	71
6.1.3. Collective step input	72
6.1.4. Deceleration maneuver	73
6.2. Open loop simulations with an improved model	75
7. Concluding remarks	77
Bibliography	79
A. Understanding the meaning of the RMA poles	87

List of Figures

3.1. Effect of parameter <i>nleak</i> on extracted pitching moment vs longitudinal displacement transfer function, QS model with static inflow.	21
3.2. A quadratic chirp with a frequency band from 0 to 44 rad/s: time history on the left, discrete Fourier transform module on the right.	23
3.3. Rational matrix approximation of aeroelastic transfer functions in hovering flight.	36
3.4. Rational matrix approximation of aeroelastic transfer functions in forward flight.	37
3.5. Aeroelastic transfer functions, BEM vs QS aerodynamics, forward flight.	38
3.6. Aeroelastic transfer functions of longitudinal-lateral dynamics coupling, forward flight.	39
3.7. Thrust due to collective pitch perturbations, hovering flight. LTI vs NLTM predictions.	39
3.8. Forward flight perturbed hub loads. LTI vs NLTM time response predictions.	41
3.9. Forward flight perturbed hub loads. Spectra of LTI and NLTM predictions.	41
3.10. Hub loads response to indicial collective pitch in advancing flight. LTI vs NLTM predictions.	42
3.11. Comparison of outputs δf and δf_s . Pitching moment M_y vs a horizontal velocity perturbation U (left), and vertical force F_z vs collective pitch perturbation θ_0 (right).	44
3.12. Heatmap of the median relative error committed by neglecting the additional states dynamics for a low frequency input.	45

List of Figures

4.1. Harmonic transfer functions relating the rolling moment with the collective pitch input.	54
4.2. Time-marching response of the aerodynamic rolling moment to a collective pitch chirp input, spanning from 0 to 70 rad/s. The complete signals (top) and a zoomed view (bottom)	55
4.3. Power spectral density of the time-marching response of the aerodynamic rolling moment to a collective pitch chirp input, spanning from 0 to 70 rad/s.. . . .	56
5.1. Transfer functions variation with respect to forward velocity and shaft angle. Sampled vs interpolated amplitude frequency distribution.	63
5.2. Influence of flight parameters on poles of identified aeroelastic ROM.	64
5.3. Comparison between interpolated and sampled transfer functions for flight conditions not included in the database.	65
5.4. Response to periodic lateral cyclic pitch. ROM vs NLTM.	66
5.5. Time histories of flight parameters during maneuver	66
5.6. Time histories of hub loads during maneuver flight. ROM vs NLTM.	66
6.1. Lateral step input at 50 kt.	69
6.2. Longitudinal cyclic step input at 50 kt.	70
6.3. Collective step input at 60 kt.	72
6.4. Deceleration with blade flap, lag and torsional modes.	73
6.5. Deceleration with one blade flapping mode.	74
6.6. Lateral step input at 60 kt	76
6.7. Acceleration from 0 to 100 kt.	76

List of Tables

3.1. Pole locus of the aeroelastic modes with a frequency less than 15 Hz	43
6.1. Performed maneuvers	68

1. Introduction

The scope and usefulness of a flight simulator goes well beyond its pilot training capabilities; indeed, simulators play an important role during the design process of vehicles and control systems. The ability of a simulator to accurately predict the behavior of a helicopter using as information only its physical characteristics would be highly desirable as it would allow manufacturers to get an early feedback from pilots on any design decision (concerning, for instance, handling qualities, rotorcraft-pilot coupling proneness, etc.). However, despite the complexity and the use of state-of-the-art components in modern simulators, they are not yet able to provide a fully coherent representation of reality [PWP⁺13]. Moreover, with the aim of correcting some sub-optimal behavior in specific flight conditions and to respect the tolerances needed for the validation of a flight model, a certain amount of artificial tuning is often applied on top of the physical model. These modifications are often not justified from an engineering standpoint and, while improving simulations for particular operating conditions, they may have an adverse effect on other parts of the flight envelope [PWP⁺13].

The need to tune the model can often be related to the deficiencies of the mathematical model describing the helicopter dynamics. The physics involved is indeed the result of the coupling of complex phenomena like the nonlinear structural dynamics of the slender main rotor blades, the complex rotor aerodynamic environment resulting from the combination of blade motion and inflow induced by wake vorticity remaining in close proximity of the rotor disk, the interaction of the air flow with the fuselage, the main and tail rotors and mutual interactions, the interaction with the ground, the dynamics of engine and actuators, the effects of control systems. Real-time simulation of these phenomena requires a suitable trade-off between modeling accuracy and computational efficiency.

1. Introduction

Modeling and simulation of the complete aerodynamic/aeroelastic response of a helicopter rotor during arbitrary manoeuvring flight conditions is yet far from being predicted with suitable accuracy. Research in the 1990's and 2000's in the USA [BLP99, QKWB99, TC00, BL00a, BL00b, BL01, BL03] pointed out the deficiencies in current rotor wake modeling for simulator applications and suggested that inaccurate and incomplete modeling of transient dynamics of the rotor wake results in deficiencies in simulator behavior to pilot control inputs. In addition, concerning rotorcraft pilot couplings (RPC), recent research [GSMQ13, SGM⁺08, MQM⁺15] highlighted the effects that aeroelastic and wake modeling may have on pilots biodynamic response. For these reasons the ability to include wake and aeroelastic effect in simulator models is fundamental.

In this work, the focus is on the mathematical modeling of a main rotor aeroelastic operator suitable for simulators, and, more in general, on the development of a complete tool chain allowing to derive computationally efficient, reduced-order models, from complex aeroelastic solvers to be used for flight simulation tasks.

This work is structured as follows:

- in section 2 the finite-state rotor aeroelastic models employed in the remainder of this work will be introduced;
- in section 3 the methodologies developed to extract linear time invariant state-space models from an arbitrary high fidelity solvers will be described;
- in section 4 the extension of these methodologies to linear time periodic state-space models will be presented;
- in section 5 the model stitching technique will be introduced to extend the validity of the aeroelastic model in the entire helicopter flight envelope;
- in section 6 the results obtained in two simulation sessions carried out in the TU Delft's SIMONA flight simulator will be illustrated;
- finally in section 7 a series of concluding remarks and possible future developments will be presented.

2. State-space main rotor aeroelastic models

2.1. State of the art

Reduced-order (finite-state) representations of aeroelastic operators developed in the last decades, both for fixed-wing and rotary-wing problems, typically rely on the introduction of reduced-order (finite-state) models for the unsteady aerodynamic operator (see, for instance, [HTD99, HP93, KNB04, GCM00, GG08]) and are suited for aeroelastic stability analysis.

Conversely, the proposed methodology provides a finite-state model relating inputs and outputs of an arbitrary-fidelity rotor aeroelastic operator, without requiring simplifications of the aerodynamic contribution: as such, it cannot be applied for rotor stability analysis (blade degrees of freedom do not appear explicitly, as detailed below), but it is applicable for rotorcraft aeromechanic analysis. Indeed, this novel state-space aeroelastic modeling is suited for simulating helicopter flight dynamics, and may be conveniently used for stability analysis and control synthesis purposes, as well as for real-time simulations [GPPG14, GGP⁺15] as it will be detailed in section 5 of this work.

Currently, computational tools devoted to helicopter flight dynamics and control usually determine forces and moments transmitted by the main rotor to the airframe by coupling its dynamics with aerodynamic loads evaluated through sectional formulations combined with wake inflow models. In that framework, wake inflow provides the important three-dimensional wake vorticity effects on rotor aerodynamics, significantly affecting the accuracy of the prediction tools. For stability and con-

2. State-space main rotor aeroelastic models

trol synthesis purposes, as well as for real-time simulations, state-space wake inflow modeling is employed. Several models have been developed in the last decades: among them, the Pitt-Peters dynamic inflow model [Pit80, PP81] is widely used by rotorcraft researchers and designers. It relates rotor loads (thrust, roll moment, and pitch moment) to the coefficients of a linear distribution of wake inflow over the rotor disc, as derived from an unsteady, actuator-disc theory. More recently, further extensions taking into account wake distortion effects have been proposed [KPP99, ZPP04], along with methodologies for extracting finite-state inflow dynamics models from simulations provided by high-fidelity aerodynamic solvers (thus, capable of including effects of complex aerodynamic phenomena, like interactions with bodies and wakes) [RKH⁺15, GGS⁺15].

For stability, control and real-time simulation purposes, the proposed aeroelastic model could replace the set of rotor blades dynamics equations with the associated dynamic wake inflow model, and the following evaluation of loads transmitted to the airframe.

2.2. Finite-state models description

The main rotor aeroelastic model used in throughout this work is a black box model yielding the components of hub forces and moments generated by the rotor, \mathbf{f} , as a functions of both hub motion variables \mathbf{x}_{MR} , namely three velocities U , V and W , and three angular velocities P , Q , and R , and the blade controls variables \mathbf{u}_{ctrl} . Note that, \mathbf{x}_{MR} collects hub displacements and rotations given by combination of airframe rigid-body motion and deformation, whereas \mathbf{u}_{ctrl} collects blade pitch controls (θ_0 , θ_{1c} , θ_{1s}) and, if present, it may also contains non-conventional controls like trailing-edge or gurney flaps. Furthermore, note that the output force vector, \mathbf{f} , might contain, separately, the loads transmitted through the mast (first load path) and the control loads transmitted to the swashplate through the control chain (second load path).

Three different models are studied in this work:

- a linear time invariant model describing the behavior of an heli-

2. State-space main rotor aeroelastic models

copter rotor in the neighborhood of a given flight condition;

- a linear time periodic model describing the behavior of an helicopter rotor in the neighborhood of a given flight condition;
- a model, linear with respect to the internal states, valid in the entire helicopter flight envelope obtained by applying a model stitching technique.

All these models are obtained by applying system identification techniques to high fidelity aeroelastic solvers which may include periodic and nonlinear terms, as well as time-delayed unsteady aerodynamics contributions due to wake vorticity (and, if considered, flow compressibility) effects. First, the transfer function matrices relating hub loads to hub motion and controls are sampled through the evaluation of a suited set of time-marching aeroelastic responses predicted by the high-fidelity aeroelastic solver (model extraction). Then a state-space representation of the loads transmitted to the airframe (model reduction) is obtained. The details of how these two steps are carried out are given in section 3 while a general description of them is given below.

2.2.1. Linear time invariant aeroelastic model

The first embodiment of the aeroelastic model under analysis is represented by a linear time invariant (LTI) system. It describes the linearized behavior of an helicopter rotor in the neighborhood of a given flight condition. It yields the perturbation components of hub forces and moments generated by the rotor, δf , as functions of perturbation of the input vector δu introduced in the previous section. All the time periodic effects are neglected. Indeed, LTI rotor representations are computationally efficient approximations of the rotor dynamics effects when relating fixed-frame variables, for which the time-constant assumption usually acceptable.

This particular model has been effectively applied by the research team of the Department of Engineering of Roma Tre University within the European project ARISTOTEL (2010-2013), aimed at defining appropriate tools for prediction of proneness of modern aircraft and rotorcraft to

2. State-space main rotor aeroelastic models

adverse pilot coupling (A/RPC), and identifying guidelines to designers of next generation aircraft to avoid it [PMD⁺11, PJDV⁺13, GCS⁺13].

Due to its LTI nature it is possible to represent the system using a transfer function matrix $\mathbf{E}(s)$ relating the outputs $\delta \mathbf{f}$ with the inputs $\delta \mathbf{u}$:

$$\delta \tilde{\mathbf{f}}(s) = \mathbf{E}(s) \delta \tilde{\mathbf{u}}(s) \quad (2.1)$$

where s is the Laplace domain variable and the $\delta \tilde{\mathbf{f}}$ and $\delta \tilde{\mathbf{u}}$ represent the Laplace transformed output and input signals respectively. In turn it is possible to represent this transfer function using the following non-proper realization [SCG14]:

$$\mathbf{E}(s) = s^2 \mathbf{D}_2 + s \mathbf{D}_1 + \mathbf{D}_0 + \mathbf{C}(s\mathbf{I} - \mathbf{A})^{-1} \mathbf{B} \quad (2.2)$$

or, alternatively, with the following state space system:

$$\begin{cases} \delta \dot{\mathbf{f}} = \mathbf{D}_2 \delta \ddot{\mathbf{u}} + \mathbf{D}_1 \delta \dot{\mathbf{u}} + \mathbf{D}_0 \delta \mathbf{u} + \mathbf{C} \mathbf{r} \\ \dot{\mathbf{r}} = \mathbf{A} \mathbf{r} + \mathbf{B} \delta \mathbf{u} \end{cases} \quad (2.3)$$

Matrices \mathbf{D}_2 , \mathbf{D}_1 , \mathbf{D}_0 , \mathbf{C} , \mathbf{A} and \mathbf{B} are real valued and are parametrized as detailed in section 3.2.1. The vector \mathbf{r} collects the additional states associated to poles of the realization. A subset of these additional states represents the blades degrees of freedom included in the high-fidelity aeroelastic solver whose dynamics falls within the considered frequency range of interest, thus affecting the extracted aeroelastic transfer matrices (see appendix A). The remaining additional states take into account flow-memory (delay) effects due to unsteady wake vorticity (and flow compressibility, if included in the analysis), that are responsible for the transcendental nature of the aerodynamics transfer functions (thus, in principle, giving rise to an infinite-dimension, state-space problem) [The49]. These observations suggest that the proposed model can be also considered as a reduced-order representation of main rotor effects on helicopter dynamics.

2. State-space main rotor aeroelastic models

2.2.2. Linear time periodic aeroelastic model

The linear time invariant model introduced in 2.2.1 is based on the hypothesis that the periodicity of the aeroelastic operator can be neglected. While this hypothesis is valid for most flight mechanics applications, there are some cases where being able to model the higher order effects caused by the time periodic behavior of the rotor is required.

A linear time periodic (LTP) model is therefore introduced. Whether for time invariant systems the concept of transfer function matrix was employed to describe the multiple input/multiple output dynamics of the aeroelastic operator, to model the time periodic effects the concept of harmonic transfer function (HTF) matrix [WH90] has to be introduced. The HTF matrix $\mathbf{G}(s)$ employed in this work, explained more in detail in section 4, relates the input $\delta \mathbf{u}$ with an arbitrary number n_h of harmonic components of the output $\delta \mathbf{f}$, defined as:

$$\delta \mathbf{f}(t) = \delta \mathbf{f}_0(t) + \sum_{k=1}^{2n_h} [\delta \mathbf{f}_{kc}(t) \cos(k\Omega_p t) + \delta \mathbf{f}_{ks}(t) \sin(k\Omega_p t)] \quad (2.4)$$

Matrix $\mathbf{G}(s)$ is formed by $m = 2n_h + 1$ blocks with dimension $M \times N$, where M is the number of outputs and N the number of inputs:

$$\mathbf{G}(s) = \begin{bmatrix} \mathbf{G}_{0,0}(s) \\ \mathbf{G}_{1c,0}(s) \\ \mathbf{G}_{1s,0}(s) \\ \vdots \\ \mathbf{G}_{n_h c,0}(s) \\ \mathbf{G}_{n_h s,0}(s) \end{bmatrix} \quad (2.5)$$

These blocks can be seen as linear time invariant transfer function matrices, each one relating the input $\delta \mathbf{u}$ with a specific component of $\delta \mathbf{f}$:

$$\delta \tilde{\mathbf{f}}_0 = \mathbf{G}_{0,0} \delta \tilde{\mathbf{u}}, \quad \tilde{\mathbf{f}}_{kc} = \mathbf{G}_{kc,0} \delta \tilde{\mathbf{u}}, \quad \delta \tilde{\mathbf{f}}_{ks} = \mathbf{G}_{ks,0} \delta \tilde{\mathbf{u}}, \quad \text{for } k = 1 \dots n_h. \quad (2.6)$$

By grouping the harmonic components of the forces in a vector $\delta \tilde{\mathbf{f}}_h$:

$$\delta \tilde{\mathbf{f}}_h = \left\{ \delta \tilde{\mathbf{f}}_0 \quad \delta \tilde{\mathbf{f}}_{1c} \quad \delta \tilde{\mathbf{f}}_{1s} \quad \dots \quad \delta \tilde{\mathbf{f}}_{n_h c} \quad \delta \tilde{\mathbf{f}}_{n_h s} \right\}^T \quad (2.7)$$

2. State-space main rotor aeroelastic models

it is possible to express the time periodic system dynamics as a linear time invariant system:

$$\delta \tilde{\mathbf{f}}_h(s) = \mathbf{G}(s) \delta \tilde{\mathbf{u}}(s) \quad (2.8)$$

It is worth noting that this system has more outputs than the LTI aeroelastic model defined in 2.2.1, in particular it has $m \cdot M$ outputs instead of M ; the number of inputs is the same. Moreover the transfer function matrix defined by the block is represents the LTI behavior of the system and it is indeed equal to \mathbf{E} [LPL14]:

$$\mathbf{G}_{0,0}(s) = \mathbf{E}(s). \quad (2.9)$$

Given that \mathbf{G} is assimilable to a transfer function a finite-state representation can be identified to obtain a time domain model:

$$\begin{cases} \delta \mathbf{f}_h = \mathbf{D}_2 \delta \ddot{\mathbf{u}} + \mathbf{D}_1 \delta \dot{\mathbf{u}} + \mathbf{D}_0 \delta \mathbf{u} + \mathbf{C} \mathbf{r} \\ \dot{\mathbf{r}} = \mathbf{A} \mathbf{r} + \mathbf{B} \delta \mathbf{u} \end{cases} \quad (2.10)$$

The time periodic output is then rebuilt by using equation 2.4.

2.2.3. Full flight envelope model

The LTI and LTP models introduced In 2.2.1 and 2.2.2, being linear, are valid in a limited neighborhood of the selected flight condition. As such they are not adequate for predicting rotor aeroelastic responses within the whole flight envelope of interest for flight simulation purposes, namely, when pilot controls and helicopter motion cannot be considered as small perturbations with respect to a reference flight condition.

In order to overcome such limit of applicability, a rotor state-space model, in which the output forces \mathbf{f} and the input controls \mathbf{u} are not perturbation values but the actual values, is proposed here. Starting from the LTI model of equation 2.3 it is possible to obtain the full values of the hub

2. State-space main rotor aeroelastic models

forces by adding the equilibrium force vector \mathbf{f}_0 to the output:

$$\mathbf{f} = \mathbf{f}_0 + \delta \mathbf{f}. \quad (2.11)$$

A set of flight parameters that suitably characterize the rotor behavior is then identified, and a parameter vector ζ containing these parameters is defined. For example, for the simulations presented in section 6 of this work these parameters were related strictly related to some of the input variables \mathbf{u} (namely the hub velocities U and W); however any external parameter of interest may be used, for example the distance from the ground (to take into account the ground effects), the rotor angular velocity (if the rotor model is coupled with an engine model), or the air density ρ_0 . This parameter vector is then used to build a database of LTI models identified in the parameter space spanned by ζ and, by using the model stitching technique presented in section 5, an expression continuously defining the LTI transfer functions for all the conditions spanned by ζ is obtained:

$$\mathbf{E}(s, \zeta) = s^2 \mathbf{D}_2(\zeta) + s \mathbf{D}_1(\zeta) + \mathbf{D}_0(\zeta) + \mathbf{C}(\zeta) [s\mathbf{I} - \mathbf{A}(\zeta)]^{-1} \mathbf{B}(\zeta) \quad (2.12)$$

where the matrices \mathbf{D}_2 , \mathbf{D}_1 , \mathbf{D}_0 , \mathbf{C} , \mathbf{A} and \mathbf{B} are now a function of the ζ . The use of this model in the time domain is explained in the details in section 5.1; to summarize, the resulting dynamical system can be expressed with the following equation:

$$\begin{cases} \mathbf{f} = \mathbf{f}_0(\zeta) + \mathbf{D}_2(\zeta) \delta \mathbf{u}(\zeta) + \mathbf{D}_1(\zeta) \delta \dot{\mathbf{u}}(\zeta) + \mathbf{D}_0(\zeta) \delta \mathbf{u}(\zeta) + \hat{\mathbf{C}}(\zeta) \dot{\mathbf{r}} \\ \dot{\mathbf{r}} = \mathbf{A}(\zeta) \mathbf{r} + \mathbf{B}(\zeta) \mathbf{u} \end{cases} \quad (2.13)$$

As mentioned before, if the parameter vector depends on the input vector, and usually such is the case, the model becomes nonlinear with respect to \mathbf{u} . For this reason it can be used to perform seamless real-time simulations for a wide range of flight conditions. The main limit of this model is its linearity with respect to the internal state vector \mathbf{r} . Indeed the additional state dynamics, albeit dependent on the flight condition through ζ and in turn \mathbf{u} , it is in any case linear in \mathbf{r} . This limitation is mitigated by using a wide parameter space for the definition of $\mathbf{A}(\zeta)$.

2.3. High fidelity models description

This section contains a brief description of the high fidelity solvers used for the finite-state model extraction throughout this work. Note that the term “high fidelity” is used here to indicate any numerical solver capable of describing the nonlinear and periodic nature of the helicopter physics, but incapable of being run in real-time due to its computational costs.

The structural solver used to model the blades dynamics, and common to all the aeroelastic models, is based on the work of Hodges and Dowell [HD74]. The aeroelastic integro-differential system of equations obtained by coupling it with aerodynamic loads is spatially integrated through the Galerkin approach, with elastic axis deformation and cross-section torsion represented as linear combinations of shape functions satisfying homogeneous boundary conditions. This yields a set of nonlinear, ordinary differential equations of the type

$$\mathbf{M}(t) \ddot{\mathbf{q}} + \mathbf{C}(t) \dot{\mathbf{q}} + \mathbf{K}(t) \mathbf{q} = \mathbf{f}_{\text{str}}^{\text{nl}}(\mathbf{q}, t) + \mathbf{f}_{\text{aer}}(\mathbf{q}, t) \quad (2.14)$$

where \mathbf{q} denotes the vector of the Lagrangian coordinates, \mathbf{M} , \mathbf{C} , and \mathbf{K} are time-periodic, mass, damping, and stiffness structural matrices representing the linear structural terms, $\mathbf{f}_{\text{str}}^{\text{nl}}(\mathbf{q}, t)$ is the vector of the nonlinear structural contributions, and finally $\mathbf{f}_{\text{aer}}(\mathbf{q}, t)$ collects the generalized aerodynamic forces.

A time-marching Newmark- β integration scheme is employed to obtain the response of the aeroelastic system to arbitrary inputs.

Two different aerodynamic solvers are employed alternatively for the computation of the aerodynamic loads \mathbf{f}_{aer} :

- a blade element theory model based on sectional Greenberg theory, under quasi-steady (QS) approximation, coupled with an inflow model (either static, Pitt-Peters or a BEM derived dynamic inflow model [GGS⁺15]);
- a boundary element method (BEM) for the solution of a boundary integral equation, suited for the analysis of potential flows around helicopter rotors in arbitrary flight conditions, included those where strong blade-vortex interactions occur [GB07].

2. State-space main rotor aeroelastic models

All the results presented in this work are representative of a hingeless rotor, closely related to the Bo-105 main rotor, having four blades with radius $R = 4.94$ m, constant chord $c = 0.395$ m, linear twist of -8° and nominal rotational speed $\Omega = 44.4$ rad/s. More details will be given on the relevant sections.

3. Linear time invariant model extraction from high-fidelity solvers

System identification methods for the characterization of high fidelity computational aeroelastic solvers are the backbone of this work. In the present section the methods that has been developed and employed in the remainder of this work will be presented. Three main topics will be covered:

- Linear time invariant (LTI) systems and their non-parametric identification
- Linear time periodic (LTP) systems and their non-parametric identification
- Parametric identification of LTI and LTP systems

Two non-parametric linear time invariant system identification techniques will be presented, one based on single harmonic response and a second based on response of a chirp input signal. These two techniques are employed to obtain an accurate estimation of the linear time invariant behavior of a generic nonlinear time periodic dynamical system, such as the aeroelastic operator of an helicopter in forward flight.

An extension of these two methodologies for the identification of linear time periodic systems will be then introduced, to be applied when the time periodic behavior can not be neglected.

Finally a parametric identification methodology for the rational matrix approximation of the sampled transfer functions, valid for both LTI and LTP models, will be presented.

3.1. Linear time invariant transfer function extraction

In this section two approaches for the transfer function extraction, or in other terms the non-parametric identification of the aeroelastic rotor operator are presented. Both the described approaches are applicable under the fundamental condition that the system for which the extraction is performed is stable. In particular, regarding the isolated rotor system presented in this work the condition is its aeroelastic stability at the steady flight condition for which the transfer function matrices are identified.

As already stated, the proposed model is introduced for helicopter flight dynamics stability analysis, and is unsuited for the stability analysis of rotor blades: actually, the rotor blades degrees of freedom appear as internal -stable- states of the resulting rotor aeroelastic operator (see App. A). The approach presented thus far for the determination of main rotor aeroelastic transfer functions has been recently applied in [QTM⁺14] for the robust, pilot-in-the-loop, stability analysis of a helicopter in steady flight.

3.1.1. Single frequency excitation method

The first method used in this work to perform the transfer function extraction consists in the following steps:

1. the high-fidelity aeroelastic solver is applied to evaluate the hub loads generated by small, single-harmonic perturbations of each variable in \mathbf{u} ;
2. the harmonic components of the resulting loads having the same frequency of the input are evaluated and then, the corresponding complex values of the frequency-response functions are determined;
3. the process is repeated for a discrete number of frequencies within a defined range, so as to get adequate sampling of the frequency-response matrix, $\mathbf{E}(j\omega)$ for the specific case examined.

3. Linear time invariant model extraction from high-fidelity solvers

Indeed, operators with periodic coefficients yield multi-harmonic outputs even when forced with single-harmonic inputs. The same is usually true for nonlinear operators. By extracting from the output only the components at the same frequency of the perturbation input implies that a constant-coefficient approximation of the operators relating f to u is obtained. Moreover, by using a sufficiently small input a linearization of the operator is performed. This capability of isolating and eliminating the effects of the time periodicity of operators is the main advantage of this identification approach. Some care is however needed if particular frequencies are analyzed, namely frequencies in the set $\{1/2\Omega_p, \Omega_p, 3/2\Omega_p, 2\Omega_p, \dots\}$ where Ω_p is the periodicity of the system. More detail on this issue are given in section 4 where the theory of linear time periodic systems will be presented.

It is worth mentioning that the second step of the process, namely the determination of the harmonic components of the output, are obtained through a discrete Fourier transform of the signal. The following issues have to be taken care of to perform an accurate identification [GM12]:

- to isolate the harmonic response the period of the aeroelastic response examined starts after that the transient is vanished.
- To avoid leakage effects the period examined is chosen to be an integer multiple of the input harmonic period.
- A sufficiently long period is recorded to reduce the effects of leakage. This is particularly important for inputs whose frequency ω is comparable to, or larger than Ω_p . Indeed if a single period of perturbation is recorded the multi-harmonic output components with a frequency smaller than ω would in part leak to the DFT peak corresponding to ω thus negatively affecting the identification quality.
- If a substantial random noise is present in the output signal an ulterior increase of the length of the recording period is performed. Then a noise reduction can be performed by mediating various periodograms.

The effect of the output sampling window size is illustrated in figure 3.1, for the transfer function relating hub longitudinal displacement perturbations to pitching moment. In forward flight conditions, the output

3. Linear time invariant model extraction from high-fidelity solvers

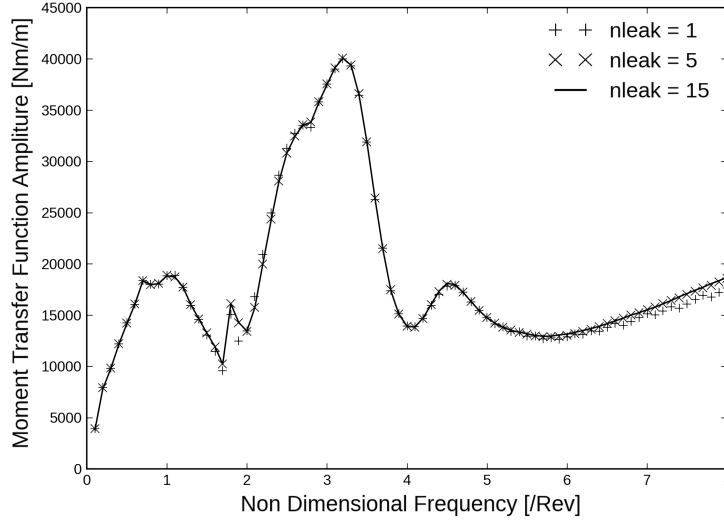


Figure 3.1.: Effect of parameter $nleak$ on extracted pitching moment vs longitudinal displacement transfer function, QS model with static inflow.

harmonic content is affected by the intrinsic periodicity of the aeroelastic operator, and this makes the size of the output sampling window a critical parameter in terms of leakage occurrence: this figure shows that, for the examined case, a five-period duration of the pulsating input is an adequate sampling window. The parameter $nleak$ represent indeed the number of sampled periods; it is worth observing that $nleak = 1$ would be adequate for a hovering rotor condition.

This method, if correctly implemented, offers a very robust approach for the non-parametric identification of the LTI transfer functions of a time-periodic system: it automatically deals with time-periodicities and most nonlinearities, and it can deal with a noisy output as well. However these features may comes at a price; the need for the extinction of the transient and the length of the recorded periods may rapidly increase the computational cost of the identification when applied to system with a large time constant (thus a long transient) and/or with particularly noisy output. Furthermore it is worth noting that the computational cost increase as $O(N_f)$ where N_f represents the number of analyzed frequencies. For this reason in the next section a method with a smaller computational cost, yet more brittle, will be presented.

3. Linear time invariant model extraction from high-fidelity solvers

3.1.2. Chirp excitation method

In the previous section the advantages of an identification technique based of single frequency excitation were discussed. However this approach has an important drawback: it usually requires long simulations to be able to sample a wide spectrum of frequencies. In fact to get a single sample of a column of the transfer function matrix (the effect of an input on all the outputs) for a certain frequency ω , a simulation time larger than the slowest time constant is needed for the transient effects to become negligible. As the value of ω increases the useful part of simulation time (proportional to $1/\omega$) becomes comparable or even smaller than the the time spent on waiting for the transient to vanish.

To overcome this efficiency issue an approach often used in system identification is perturbing the system with more than one frequency at a time. The approach presented in this section uses a so called “chirp” signal as an input. This methodology is widely used in [TR06] for the identification of rotorcraft and aircraft systems, and in this section the same approach will be presented. However, it will be shown that this approach is not suitable for the identification of the rotor aeroelastic operator under analysis due its inability to cope with time periodic effects. An extension for the robust application to LTP systems will be presented in section 4.2.1.

The main characteristic of a chirp signal is the full band spectrum. This characteristic is shared with impulse inputs with the advantage of having a much smaller maximum amplitude of the signal for the same frequency spectrum module; a small amplitude of the signal is fundamental when a linear behavior of the system is sought as in the present case.

A simple chirp signal can be defined as an harmonic signal whose frequency varies in time. For example:

$$u(t) = \sin(g(t)t + \phi) \quad (3.1)$$

where the function $g(t)$ defines how the frequency is swept along the chirp. In particular the frequency $\omega(t)$ can be defined taking the first

3. Linear time invariant model extraction from high-fidelity solvers

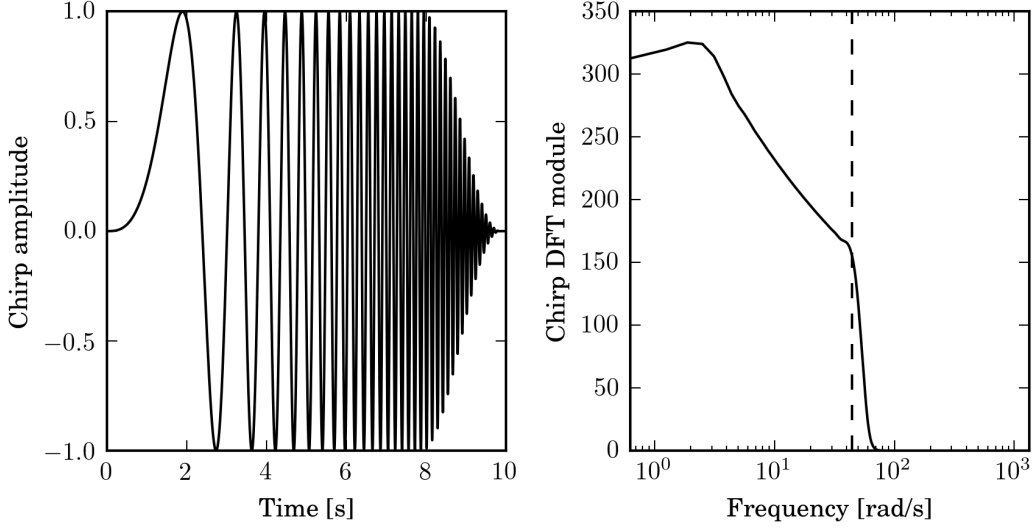


Figure 3.2.: A quadratic chirp with a frequency band from 0 to 44 rad/s: time history on the left, discrete Fourier transform module on the right.

derivative of $g(t)t$:

$$\omega(t) = \frac{d}{dt} [g(t)t] = t \frac{d}{dt} g(t) + g(t). \quad (3.2)$$

In real applications the chirp spectrum is limited in a band between a minimum and a maximum frequency and it depends on the choice of the frequency function $g(t)$. Moreover a good practice when creating an input chirp is having a decreasing amplitude at the end of the signal and to zero-pad it further for at least a duration equal to the slowest dynamics of the excited system. In this way both the input and the output will be less affected by the windowing effects introduced by the discrete Fourier Transform. In figure 3.2 a quadratic chirp with this characteristics and its frequency spectrum are depicted. The dashed vertical line in the right part of that figure indicates the maximum frequency at which the system is adequately excited, while the decreasing nature of the signal band is caused by the quadratic nature of $g(t)$.

Similarly to the previous method the high-fidelity aeroelastic solver is applied to evaluate the hub loads generated by the small chirp input, for each variable in u . To proceed with the identification of the transfer functions (see [Lju98] for a complete theoretical overview) two approaches

3. Linear time invariant model extraction from high-fidelity solvers

can be employed. The simplest, yet more brittle approach relies on the discrete Fourier transform. The ratio between the DFTs of the output and of the input gives a good estimation of the transfer functions $E(j\Omega)$ when the output signal is not affected by noise and when the windowing artifacts are negligible for both signals:

$$E(j\omega_i) = \frac{\tilde{y}(j\omega_i)}{\tilde{u}(j\omega_i)} \quad (3.3)$$

While it is possible to reduce the artifacts introduced by the windowing of the signal, it is often impossible to eliminate all the noise sources from the output. Even for signals that are the outcome of a presumably deterministic computer simulation (such are all the output signals considered in this work) a certain noise component with characteristic similar to random noise is often present.

To reduce the influence of the random noise on the quality of the estimation a second approach for the analysis of the chirp output can be employed: the power spectral densities of the signals are considered instead of their DFTs [Lju98]. In particular the transfer function between an input u and an output y is defined as:

$$E(j\omega_i) = \frac{P_{yu}(\omega_i)}{P_{uu}(\omega_i)} \quad (3.4)$$

where P_{yu} and P_{uu} are the input-output cross spectral density (CSD) and the power spectral density (PSD) of the input respectively. Recalling the definition of the cross and power spectral densities it can be shown that the zero mean random noise is filtered by the application of the cross spectral density operator. On an implementation level in this work the estimation of the spectral densities is carried out using the Welch periodograms technique [Wel67]. It is worth noting that, similarly to the single frequency-response method presented previously, a noisy signal imposes a longer duration of the simulation to be able to maintain a sufficient frequency resolution due to the application of the periodogram method.

Even if longer simulation times may be able to effectively mitigate the negative effect of the noise on the identification accuracy, this method, as

3. Linear time invariant model extraction from high-fidelity solvers

presented, does not offer an effective way to filter out the multi-harmonic effects caused by nonlinearities time periodic behavior of the operator. In particular this second issue is of fundamental importance for the objectives of this work and a solution will be presented in section 4.2.1.

To obtain an indication of the quality of the identification in terms of impact of output noise and effects of certain nonlinearities the coherence between the input and the output can be used [TR06]. The coherence between two signals $u(t)$ and $y(t)$ is defined as:

$$C_{yu}(\omega_i) = \frac{|P_{yu}(\omega_i)|^2}{P_{uu}(\omega_i) P_{yy}(\omega_i)} \quad C(\omega) \in \{0, 1\} \quad (3.5)$$

and it varies between zero and one. An unitary, or almost unitary, coherence is an indication of a linear correlation between the two signals and hence it may indicate that the transfer function was correctly identified. A low coherence may indicate a high noise-to-signal ratio, the presence of certain kinds of nonlinearities, an insufficient excitation of a particular range of frequencies, or simply a zero of the system. However useful, the coherence is unable to point out the presence of time-periodic effects.

3.2. Rational matrix approximation

In modern control theory parametric system identification usually tries to find the value of the matrices¹ A , B , C and D_0 defining a proper transfer function:

$$E_p(s) = D_0 + C(sI - A)^{-1} B \quad (3.6)$$

from the knowledge of $E_p(j\omega_k)$ for a discrete number of frequencies ω_k .

In aeroelasticity non-proper transfer functions are common in the description of the aerodynamic forces with respect to generalized modes [Kar82]. Let us consider for instance the transfer function relating the forces produced by a two dimensional airfoil with its angle of attack and vertical velocity. In that case the output of the system will depend directly on the first and on the second derivatives of some inputs. To de-

¹In the control literature the constant matrix D_0 is usually referred as D .

3. Linear time invariant model extraction from high-fidelity solvers

scribe this relation a non-proper transfer function has to be used:

$$\mathbf{E}(s) = \mathbf{D}_2 s^2 + \mathbf{D}_1 s + \mathbf{D}_0 + \mathbf{C}(s\mathbf{I} - \mathbf{A})^{-1} \mathbf{B} \quad (3.7)$$

where matrices \mathbf{D}_1 , \mathbf{D}_2 deals with the linear dependency of the output on the first and on the second time derivative of the input respectively. In fact if we consider the canonical input-output relation defined by the transfer function matrix $\mathbf{E}(s)$ in the Laplace domain:

$$\tilde{\mathbf{y}}(s) = \mathbf{E}(s) \tilde{\mathbf{u}}(s) \quad (3.8)$$

when it is transformed back in the time domain it becomes the following dynamical system:

$$\begin{aligned} \dot{\mathbf{r}} &= \mathbf{A}\mathbf{r} + \mathbf{B}\mathbf{u} \\ \mathbf{y} &= \mathbf{C}\mathbf{r} + \mathbf{D}_0\mathbf{u} + \mathbf{D}_1\dot{\mathbf{u}} + \mathbf{D}_2\ddot{\mathbf{u}} \end{aligned} \quad (3.9)$$

When matrix \mathbf{D}_2 and \mathbf{D}_1 are null the transfer function is proper again. Matrices \mathbf{D}_2 , \mathbf{D}_1 and \mathbf{D}_0 define the polynomial part of the transfer function $\mathbf{E}(s)$ while matrices \mathbf{C} , \mathbf{A} and \mathbf{B} form the rational part of the transfer function. As discussed in detail in the following paragraphs, the estimation of the matrices forming the rational part represents the main challenge of the parametric identification. For this reason the procedure is also called rational matrix approximation or RMA.

In the previous sections a methodology to sample transfer function matrices $\mathbf{E}(j\omega)$ (or alternatively $\mathbf{G}(j\omega)$ for HTF matrices) from numerical solvers was introduced. In this section this information will be used to obtain the values of the matrices \mathbf{D}_2 , \mathbf{D}_1 , \mathbf{D}_0 , \mathbf{C} , \mathbf{A} and \mathbf{B} . Before presenting the rational matrix approximation approach developed for this work it is worth highlighting the challenges posed by the parametric identification.

3.2.1. Parametrization of the state-space matrices

The first step in the parametric identification is the definition of the parameters defining the matrices \mathbf{D}_2 , \mathbf{D}_1 , \mathbf{D}_0 , \mathbf{C} , \mathbf{A} and \mathbf{B} . If some char-

3. Linear time invariant model extraction from high-fidelity solvers

acteristics of the system under analysis are known it may be possible to reduce the number of parameters defining these matrices. For the cases analyzed in this work scarce or no prior information are available to define a specific parametric model. Moreover a general parametric model was sought to be able to describe any aerodynamic and aeroelastic effects.

A parametrization of a state space model is a mapping from the parameter space to the rational transfer function space. Two important features of a parametrization are its injectivity and its surjectivity. Recalling some basic properties of mappings, we define a parametrization as injective if any rational transfer function in the parametrization range can be described by only one parameter vector. Similarly a parametrization is surjective if the entire rational transfer function space is spanned by the map, that is any function can be represented by at least one parameter vector. If a mapping is both injective and surjective it is called bijective; however, while for SISO systems bijective parametrizations are often used, for MIMO systems it was shown [Gui75, Lue67] that there are no such parametrizations.

Considering the state space form of Eq. 3.7, following [Cla76] the theoretical minimum number of parameters necessary to define all the possible rational transfer function for a dynamical system with McMillian degree p is:

$$d_{\min} = p(m + n) + 3mn \quad (3.10)$$

while the total number of matrix coefficients is $p^2 + p(m + n) + 3mn$.

A further fundamental characteristic of a parametrization is the possibility to impose the asymptotic stability of the model.

On the topic of the choice of parametrization there is an extensive literature and the review of the various options is outside the scope of this work. Only the two parametrizations employed in this work will be described in detail: the tridiagonal parametrization and the block-diagonal parametrization.

The tridiagonal parametrization is a well known surjective parametrization. It is based on the notion (see e.g. [GVL12]) that any real square A matrix can be transformed to a tridiagonal matrix \hat{A} using a similarity

3. Linear time invariant model extraction from high-fidelity solvers

transformation:

$$\hat{A} = \mathbf{T}^{-1} \mathbf{A} \mathbf{T} \quad (3.11)$$

In fact, considering the rational part of equation 3.7, it is possible to define two matrices $\hat{\mathbf{B}} = \mathbf{T}^{-1} \mathbf{B}$ and $\hat{\mathbf{C}} = \mathbf{C} \mathbf{T}$ such that matrix \mathbf{A} can be substituted by any matrix $\hat{\mathbf{A}}$ similar to it:

$$\mathbf{C} (s\mathbf{I} - \mathbf{A})^{-1} \mathbf{B} = \mathbf{C} \mathbf{T} (s\mathbf{I} - \hat{\mathbf{A}})^{-1} \mathbf{T}^{-1} \mathbf{B} = \hat{\mathbf{C}} (s\mathbf{I} - \hat{\mathbf{A}})^{-1} \hat{\mathbf{B}} \quad (3.12)$$

The standard tridiagonal parametrization has:

$$d_{\text{tri}} = p(3 + m + n) - 2 + 3mn \quad (3.13)$$

parameters, with the matrix \mathbf{A} defined as:

$$\mathbf{A}(\theta) = \begin{bmatrix} \theta_1 & \theta_2 & 0 & 0 & 0 \\ \theta_3 & \theta_4 & \theta_5 & 0 & 0 \\ 0 & \theta_6 & \theta_7 & \theta_8 & 0 \\ 0 & 0 & \theta_9 & \theta_{10} & \ddots \\ 0 & 0 & 0 & \ddots & \ddots \end{bmatrix} \quad (3.14)$$

In [MH96] a compact tridiagonal parametrization was proposed to further reduce the number of parameters to:

$$d_{\text{c-tri}} = p(2 + m + n) - 1 + 3mn \quad (3.15)$$

by using the following parametrization for matrix \mathbf{A}

$$\mathbf{A}(\theta) = \begin{bmatrix} \theta_1 & \theta_2 & 0 & 0 & 0 & 0 \\ \theta_3 & \theta_1 & \theta_4 & 0 & 0 & 0 \\ 0 & 0 & \theta_5 & \theta_6 & 0 & 0 \\ 0 & 0 & \theta_7 & \theta_5 & \theta_8 & 0 \\ 0 & 0 & 0 & 0 & \theta_9 & \ddots \\ 0 & 0 & 0 & 0 & \ddots & \ddots \end{bmatrix} \quad (3.16)$$

while keeping the full parametrization for both \mathbf{B} and \mathbf{C} .

By sacrificing the surjectivity of the parametrization it is possible to drop

3. Linear time invariant model extraction from high-fidelity solvers

the even superdiagonal elements $\theta_4, \theta_8, \dots, \theta_{4i}$ of \mathbf{A} . In fact these elements are necessary only to represent non-diagonalizable matrices, while any real matrix with unitary geometric multiplicity of eigenvalues can be represented by a block diagonal matrix with 2x2 blocks.

In [MF05] a parametrization based on a block diagonal representation of \mathbf{A} was presented. In particular matrix \mathbf{A} was defined as:

$$\mathbf{A}(\theta) = \begin{bmatrix} \theta_1 & -\theta_2 & 0 & 0 \\ \theta_2 & \theta_1 & 0 & 0 \\ 0 & 0 & \theta_3 & -\theta_4 \\ 0 & 0 & \theta_4 & \theta_3 \end{bmatrix} \quad (3.17)$$

with its eigenvalues readily identified as:

$$\lambda_i = \theta_i \pm j\theta_{i+1}. \quad (3.18)$$

With this parametrization it is very easy to impose the asymptotic stability of the model, but on the other hand it is neither injective nor surjective. The total number of parameters of the block-diagonal parametrization is the following:

$$d_{\text{b-diag}} = p(m + n + 1) + 3mn. \quad (3.19)$$

One of the problems of this parametrization is that distinct real eigenvalues can not be easily represented. For the applications for which it was developed this limitation was not significant as usually all the eigenvalues were complex conjugate. However, for the sake of completeness a modification of it is hereby proposed to be able to work with real eigenvalues.

The same spanned range of the previous parametrization is shared by this one, but the behavior regarding real poles is improved. The matrix

3. Linear time invariant model extraction from high-fidelity solvers

\mathbf{A} is defined as:

$$\mathbf{A}(\theta) = \begin{bmatrix} \theta_1 & -\theta_2 & 0 & 0 & 0 \\ |\theta_2| & \theta_1 & 0 & 0 & 0 \\ 0 & 0 & \theta_3 & -\theta_4 & 0 \\ 0 & 0 & |\theta_4| & \theta_3 & 0 \\ 0 & 0 & 0 & 0 & \theta_5 \end{bmatrix}. \quad (3.20)$$

and its eigenvalues are:

$$\lambda_i = \theta_i \pm \sqrt{\theta_{i+1}} \sqrt{|\theta|_{i+1}}. \quad (3.21)$$

Imposing the asymptotic stability in this case is not as straightforward as the previous parametrization but neither is particularly difficult. On the other hand, distinct real poles can be represented easily.

All the parametrizations above introduced focused on reducing the number of parameters defining the matrix \mathbf{A} by using similar transformations. So far matrices \mathbf{C} and \mathbf{B} are considered fully parametrized. In the following a procedure to reduce the number of parameters defining matrix \mathbf{C} is presented.

For every square matrix \mathbf{A} it is possible to define a set of transformation matrices \mathbf{R} , having the same eigenvectors of \mathbf{A} , such that:

$$\mathbf{R}^{-1}\mathbf{A}\mathbf{R} = \mathbf{A}. \quad (3.22)$$

To show this property let us consider the diagonalized form of both matrices:

$$\mathbf{A} = \mathbf{Z}\mathbf{\Lambda}_A\mathbf{Z}^{-1} \quad \mathbf{R} = \mathbf{Z}\mathbf{\Lambda}_R\mathbf{Z}^{-1}. \quad (3.23)$$

Substituting Eqs. 3.23 in Eq. 3.22 and exploiting the commutativity of diagonal matrices it is trivial to prove the equivalence of Eq. 3.22:

$$\mathbf{R}^{-1}\mathbf{A}\mathbf{R} = \mathbf{Z}\mathbf{\Lambda}_R^{-1}\mathbf{Z}^{-1}\mathbf{Z}\mathbf{\Lambda}_A\mathbf{Z}^{-1}\mathbf{Z}\mathbf{\Lambda}_R\mathbf{Z}^{-1} = \mathbf{Z}\mathbf{\Lambda}_R^{-1}\mathbf{\Lambda}_A\mathbf{\Lambda}_R\mathbf{Z}^{-1} = \mathbf{A}. \quad (3.24)$$

Matrices \mathbf{A} and \mathbf{R} are said to be simultaneously diagonalizable matrices; however it is worth noting that this property is valid also for non-diagonalizable matrices using generalized eigenvectors, as Jordan blocks satisfy the commutative property as well as diagonal matrices.

3. Linear time invariant model extraction from high-fidelity solvers

Considering the rational part of Eq. 3.7 it is possible to obtain the same rational transfer function using different C and B matrices but keeping the same A by simply pre- and post-multiplying A by any simultaneously diagonalizable matrix R :

$$C(sI - A)^{-1}B = CR^{-1}(sI - A)^{-1}RB = \tilde{C}(sI - A)^{-1}\tilde{B} \quad (3.25)$$

This non uniqueness of definition of C and B leads to a bad numerical conditioning of the least square optimization problem as the Hessian matrix becomes singular [VV07] due to the local non injectivity of the map. To solve this issue the number of parameters defining one of the two matrices can be reduced by using the following procedure exploiting the aforementioned properties of the simultaneously diagonalizable matrices in the following way. Considering the separable nonlinear least square procedure used for the optimization of the parameters (see section 3.2.2) a reduced parametrization of matrix C is sought. This matrix can be rewritten as:

$$\tilde{C}(\tilde{\theta}) = C(\theta)R \quad (3.26)$$

where C is fully parametrized while \tilde{C} depends on a parameter vector $\tilde{\theta}$ that is at most p elements smaller than the full parameter vector θ . In general the parametrization of \tilde{C} has to be chosen to be reachable for every C and for every obtainable $A(\theta)$. In fact it must be kept in mind that R depends on A , as they must share the same eigenvectors, and on p parameters, namely its eigenvalues².

Matrix R can be seen as obtained by summing p matrices of unitary rank:

$$R = \sum_i^p \lambda_i \mathbf{q}_i \mathbf{z}_i^T \quad (3.27)$$

where the vectors \mathbf{q}_i and \mathbf{z}_i represent the i -th column of matrices Z^{-1} and Z^T respectively. Considering that R has full rank it follows that for every eigenvalue λ_i of R there exist at least a row and a column of that matrix having at least a coefficient depending linearly on λ_i . For this reason, under certain conditions regarding C stated below, it is possible

²These eigenvalues are arbitrarily chosen so it is possible to assume that they are real valued.

3. Linear time invariant model extraction from high-fidelity solvers

to define a generic reduced parametrization of \tilde{C} that can be used for any parametrization of A having a fixed coefficient for every column, for instance:

$$\tilde{C}(\theta) = \begin{bmatrix} 1 & 1 & 1 & 1 \\ \theta_1 & \theta_3 & \theta_5 & \theta_7 \\ \theta_2 & \theta_4 & \theta_6 & \theta_8 \end{bmatrix} \quad (3.28)$$

However this parametrization of C is not surjective. To proof this it is sufficient to consider, for example, the first coefficient of \tilde{C} , obtained from the dot product of the first row c_1 of C and the first column r_1 of R . This coefficient was imposed to be equal to one, but in this way it is not possible to describe a matrix C having a first column orthogonal to the first row of R , thus proving the non-surjectivity of the parametrization.

One of the nice features of the block diagonal parametrization, albeit not exploited in [MF05], is that the form of matrix R is well defined, thus making it easy to define a reduced parametrization of C not suffering from its non-surjectivity. In particular R has the same form as A , that is block diagonal with 2x2 blocks depending on two independent parameters x and y :

$$\mathbf{R}_{b\text{-diag}}^{2 \times 2} = \begin{bmatrix} x & -y \\ |y| & x \end{bmatrix} \quad (3.29)$$

By employing this property the total number of parameters for the block-diagonal parametrization becomes:

$$d = p(m + n) + 3mn, \quad (3.30)$$

equal to the theoretical minimum number of parameters of Eq. 3.10.

3.2.2. Nonlinear separable least square

In this section, the numerical approach applied for the rational matrix approximation of the transfer matrix, $E(s)$, is outlined.

Once the parametrization of the matrices D_2 , D_1 , D_0 , C , A and B is chosen, as described in the section 3.2.1, the value of the parameters θ defining said matrices is sought as to minimize the following least-

3. Linear time invariant model extraction from high-fidelity solvers

square problem:

$$\min_{\mathbf{A}_2, \mathbf{A}_1, \mathbf{A}_0, \mathbf{A}, \mathbf{B}, \mathbf{C}} \left(\sum_{n=1}^{N_f} \|\mathbf{Q}(j\omega_n)\|_F^2 \right) \quad (3.31)$$

where $\|\cdot\|_F$ represents Frobenius norm of a matrix, ω_n is the discrete set of N_f frequencies at which $\mathbf{E}(s)$ is known (samples), whereas \mathbf{Q} is the error matrix defined as:

$$\mathbf{Q}(j\omega) = -\omega^2 \mathbf{D}_2 + j\omega \mathbf{D}_1 + \mathbf{D}_0 + \mathbf{C} (j\omega \mathbf{I} - \mathbf{A})^{-1} \mathbf{B} - \mathbf{E}(j\omega) \quad (3.32)$$

To solve this minimization problem several methods have been proposed in the literature [Kar82, MMDT⁺95, MF05]. The method presented in [MMDT⁺95], consisting in a single linear least-square solution approach, has been successfully applied for finite-state modelling of rotary-wing aerodynamic operators [GM12, GCM00, GG82], but numerical tests have shown that it is unsuited for the approximation of the non-smooth, irregular transfer functions characterizing helicopter main rotor aeroelastic operators. Better results have been obtained by the method presented in [MF05], which solves the minimization problem of 3.31 through an optimizer based on the conjugate gradient method. Nonetheless, it yields suboptimal solutions and is not robust enough in terms of convergence to the minimum. The minimization problem solution proposed here is an extension of the approach of [MF05], that uses the separable variables approach.

Considering equation 3.32 it can be observed that, for a given frequency ω_i , matrix \mathbf{Q} depends linearly on the polynomial contribution matrices (namely, \mathbf{D}_k for $k = 0, 1, 2$) and that, for given \mathbf{C} and \mathbf{A} matrices, it is linearly dependent also on matrix \mathbf{B} . This feature of the approximation rational form applied is exploited to separate the minimization variables into two sets, a linear least-square problem and a nonlinear one.

First, the linear set of unknown variables is defined as the solution of

3. Linear time invariant model extraction from high-fidelity solvers

the following algebraic problem derived from equation 3.32:

$$\begin{bmatrix} -\omega_1^2 \mathbf{I} & j\omega_1 \mathbf{I} & \mathbf{I} & \mathbf{C} (j\omega_1 \mathbf{I} - \mathbf{A})^{-1} \\ -\omega_2^2 \mathbf{I} & j\omega_2 \mathbf{I} & \mathbf{I} & \mathbf{C} (j\omega_2 \mathbf{I} - \mathbf{A})^{-1} \\ \vdots & \vdots & \vdots & \vdots \\ -\omega_{N_f}^2 \mathbf{I} & j\omega_{N_f} \mathbf{I} & \mathbf{I} & \mathbf{C} (j\omega_{N_f} \mathbf{I} - \mathbf{A})^{-1} \end{bmatrix} \begin{bmatrix} \mathbf{D}_2 \\ \mathbf{D}_1 \\ \mathbf{D}_0 \\ \mathbf{B} \end{bmatrix} = \begin{bmatrix} \mathbf{Q}(j\omega_1) \\ \mathbf{Q}(j\omega_2) \\ \vdots \\ \mathbf{Q}(j\omega_{N_f}) \end{bmatrix} + \begin{bmatrix} \mathbf{E}(j\omega_1) \\ \mathbf{E}(j\omega_2) \\ \vdots \\ \mathbf{E}(j\omega_{N_f}) \end{bmatrix} \quad (3.33)$$

where equation coefficients explicitly depend on the set of nonlinear variables, the unknowns are real valued (entries of matrices $\mathbf{D}_2, \mathbf{D}_1, \mathbf{D}_0$ and \mathbf{B}), whereas right hand side contributions have complex values.

Then, the set of nonlinear variables is defined as the solution of a separate reformulated nonlinear minimization problem, thus dealing with a drastically reduced size of solution domain. Indeed, rewriting 3.33 in a more compact notation as:

$$\mathbf{M} \mathbf{X}_{\text{lin}} = \hat{\mathbf{Q}} + \hat{\mathbf{H}} \quad (3.34)$$

where \mathbf{M} is the coefficient matrix, \mathbf{X}_{lin} collects the matrices of the unknown linear variables, while $\hat{\mathbf{H}}$ and $\hat{\mathbf{Q}}$ denote, respectively, transfer function and residual matrices evaluated at the sampling frequencies, the optimal value of \mathbf{X}_{lin} (linear least-square solution of 3.34) is formally given by

$$\mathbf{X}_{\text{lin}} = \mathbf{M}^* \hat{\mathbf{H}}. \quad (3.35)$$

with $\mathbf{M}^* = (\mathbf{M}^T \mathbf{M})^{-1} \mathbf{M}^T$ denoting the Moore-Penrose pseudoinverse of matrix \mathbf{M} , and the minimization problem concerning the nonlinear variables is formulated as follows

$$\min_{\mathbf{C}, \mathbf{A}} \left(\left\| \hat{\mathbf{Q}} \right\|_F^2 \right) \quad (3.36)$$

with $\hat{\mathbf{Q}}$ not depending on \mathbf{X}_{lin} , as demonstrated by the combination of equations 3.34 and 3.35, that yields

$$\hat{\mathbf{Q}} = (\mathbf{M} \mathbf{M}^* - \mathbf{I}) \hat{\mathbf{H}} \quad (3.37)$$

The nonlinear minimization problem of equation 3.36 is solved by a local minimization method based on the Broyden-Fletcher-Goldfarb-Shanno

3. Linear time invariant model extraction from high-fidelity solvers

(BFGS) algorithm [Sha70], with matrix-fraction approach of [MMDT⁺95] applied to define the initial guess solution. The gradient of the objective function required by the BFGS algorithm (namely, the partial derivatives of $f_{obj} = \|\hat{\mathbf{Q}}\|_F^2$ with respect to the parameters defining A and C) is evaluated through the method developed in [GP73]. Once the optimal solution of 3.36 is determined, 3.35 directly yields the optimal values of the linear variables.

In principle, the minimization problem should be subject to a set of constraints imposing real part of poles (namely, the eigenvalues of matrix A) to be negative (in order to let the finite-state form represent a stable system behavior, as required by initial assumptions of the proposed approach. However, it is observed that such constraints are often automatically satisfied: this may be considered as an indication of the robustness of the presented approach, which allows application of the convenient unconstrained version of the BFGS algorithm.

3.2.3. Static derivatives imposition

To improve the accuracy of the identified model, especially when low frequency inputs are analyzed, it may be convenient to exploit the knowledge of the static derivatives matrix $\mathbf{X}_{ij} = \frac{\partial f_i}{\partial u_j}$. This matrix can be easily and accurately calculated by applying to the high fidelity aeroelastic solver a small, constant valued perturbation and measuring the output variation. In other words by applying a simple numerical differentiation. It is easy to see that, as ω approaches zero, the transfer function matrix $\mathbf{E}(j\omega)$ approaches the static derivatives matrix. Recalling equation 3.7 we have:

$$\mathbf{E}(0) \equiv \mathbf{X} = \mathbf{D}_0 - \mathbf{C}\mathbf{A}^{-1}\mathbf{B} \quad (3.38)$$

This equation can be used to express matrix \mathbf{D}_0 as a function of C, A and B, thus reducing the number of unknowns in the optimization problem. Indeed if X is known the error matrix becomes:

$$\mathbf{Q}(j\omega) = -\omega^2\mathbf{D}_2 + j\omega\mathbf{D}_1 + \mathbf{C}[(j\omega\mathbf{I} - \mathbf{A})^{-1} + \mathbf{A}^{-1}]\mathbf{B} - \mathbf{E}(j\omega) + \mathbf{X} \quad (3.39)$$

This reduction of the dimensions of the optimization problem has the

3. Linear time invariant model extraction from high-fidelity solvers

twofold effect of improving reducing the computational cost needed for the parametric identification, and of improving the accuracy of the resulting model.

3.3. Numerical results

3.3.1. Transfer function identification

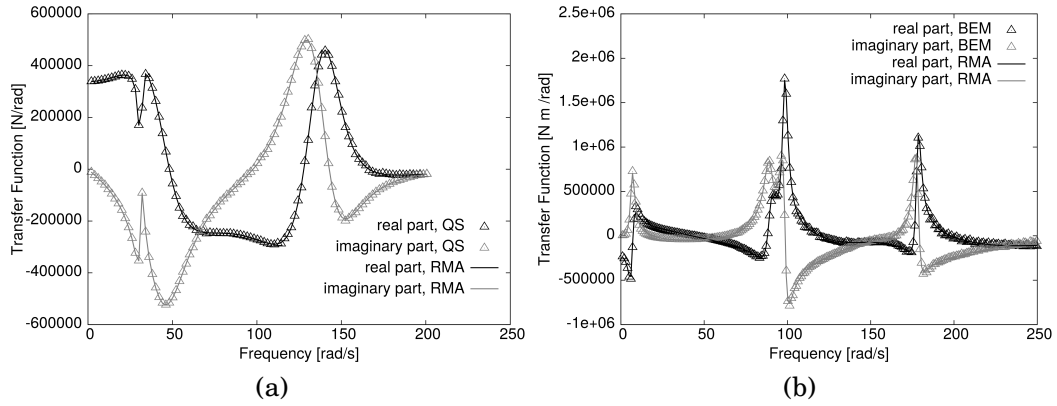


Figure 3.3.: Rational matrix approximation of aeroelastic transfer functions in hovering flight.

To give an indication of the accuracy of the parametrization method presented in this section, figures 3.3 and 3.4 present the rational approximations of transfer functions compared with sampled data, respectively for hovering and forward flight conditions. In order to demonstrate that it is possible to use the proposed method in combination with any aeroelastic solver, predictions from both BEM and sectional, QS aerodynamic solvers are considered. Specifically, for the hovering flight condition, figure 3.3a depicts the hub axial force *vs* collective pitch control perturbations evaluated by quasi-steady aerodynamics, whereas figure 3.3b illustrates the hub pitch moment *vs* longitudinal cyclic pitch perturbations evaluated by BEM aerodynamics. Transfer functions evaluated for advance ratio $\mu = 0.3$ are presented in figures 3.4a and 3.4b. They concern, respectively, hub roll moment *vs* roll angular velocity perturbations as given by QS aerodynamics and hub roll moment *vs* lateral cyclic pitch

3. Linear time invariant model extraction from high-fidelity solvers

perturbations as predicted by BEM aerodynamics. These figures demonstrate the high quality of approximation of the aeroelastic transfer functions achieved by the RMA method presented, which is an essential item of the whole process to obtain a highly-accurate final finite-state, LTI aeroelastic rotor model.

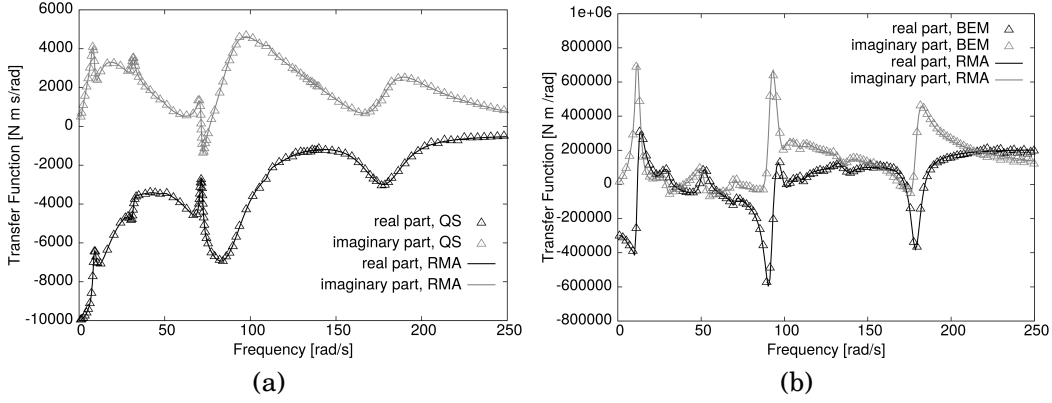


Figure 3.4.: Rational matrix approximation of aeroelastic transfer functions in forward flight.

Next, for $\mu = 0.3$, the effects of the high-fidelity aeroelastic solver accuracy on the extracted linear model are examined. Figure 3.5 shows the comparisons, in terms of amplitude and phase, between transfer functions extracted from the aeroelastic solver based on BEM aerodynamics and corresponding ones obtained by sectional aerodynamics. In particular, figure 3.5a depicts the transfer functions between the lateral force and the lateral velocity perturbations, while figure 3.5b presents the transfer functions between roll moment and roll angular velocity perturbations. In both cases, the two extracted models present poles that have very close frequency locations: this is expected, in that rotor blades structural dynamics strongly affects poles and zeros of the aeroelastic response functions. However, large discrepancies may appear on aeroelastic mode damping. This is particularly true when the dynamics is dominated by the flapping modes, which are strongly affected by aerodynamic loads modeling, as it is evident in figure 3.5b. Differently, for responses governed by the lag modes, like those depicted in figure 3.5a, the two aeroelastic solvers provides closer prediction, also in terms of mode damping. The comparisons of the rest of the transfer functions

3. Linear time invariant model extraction from high-fidelity solvers

extracted from the two considered models, not shown here for the sake of conciseness, present the same characteristics. It is worth noting that, the small damping of the flapping modes is partially related to the fact that a prescribed wake shape has been used by the BEM solver. Indeed, it has been observed that a wake model of this type tends to predict less damped wake inflow dynamics compared to free-wake modeling [GGS⁺15], thus correspondingly affecting flapping modes.

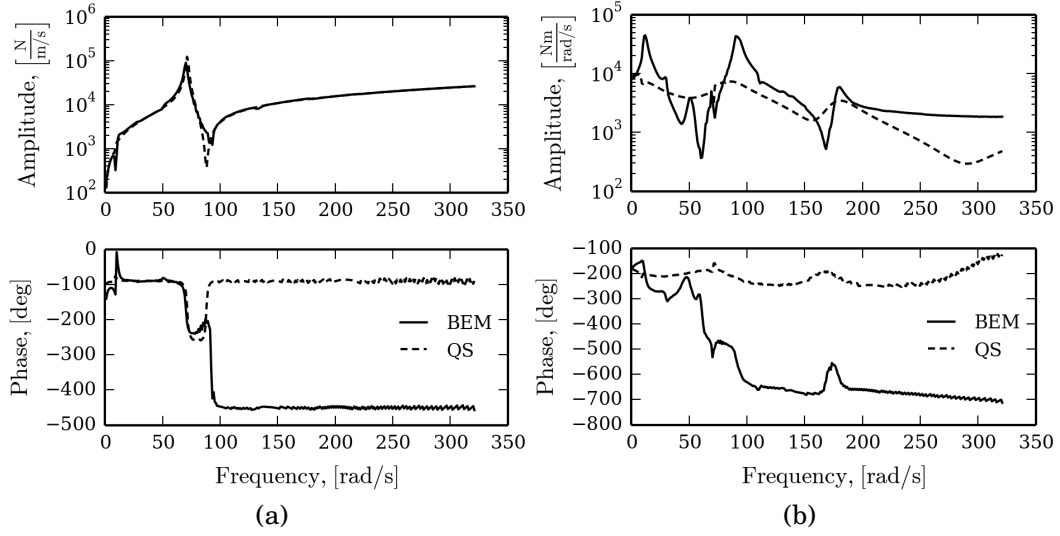


Figure 3.5.: Aeroelastic transfer functions, BEM *vs* QS aerodynamics, forward flight.

Furthermore, for the sake of completeness, some transfer functions extracted from the BEM-based aeroelastic solver that concern off-axis responses are presented in figure 3.6. Specifically, figure 3.6a depicts the transfer function between the pitch moment and the roll angular velocity perturbations, while figure 3.6b presents the transfer function between yaw moment and blade collective pitch perturbations. Compared also with the results in figure 3.5, they prove the capability of the proposed aeroelastic modeling approach to capture the significant cross-coupling effects between longitudinal and lateral dynamics that are a typical feature of rotorcraft.

3. Linear time invariant model extraction from high-fidelity solvers

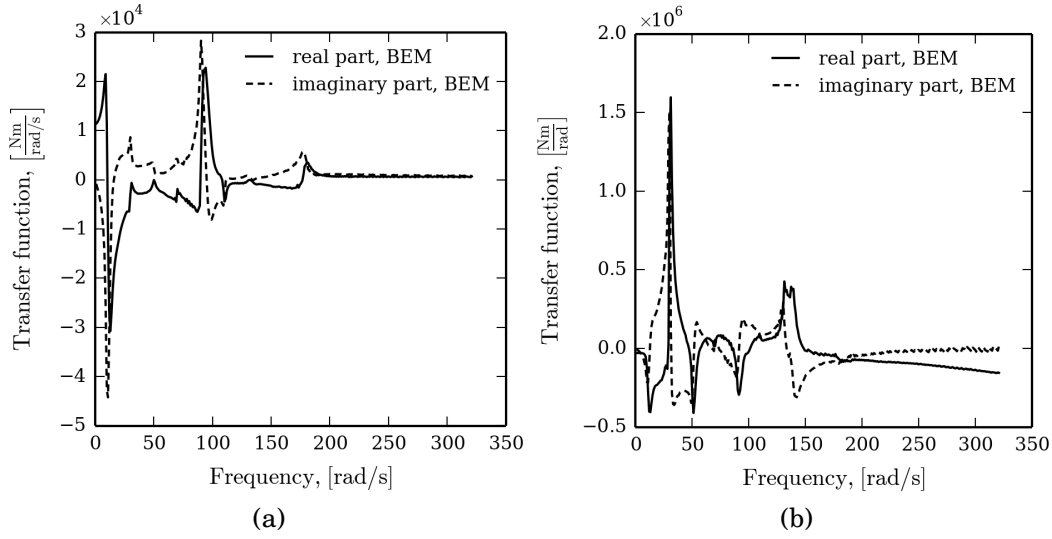


Figure 3.6.: Aeroelastic transfer functions of longitudinal-lateral dynamics coupling, forward flight.

3.3.2. Time-response analysis

The high level of accuracy of the reduced-order, aeroelastic rotor formulation proposed is proven by comparing the predicted rotor-hub perturbation forces and moments with those provided by the high-fidelity, non-linear, time-marching solver (NLTM). These loads are obtained as responses to an arbitrary blade pitch command input, θ_{com} .

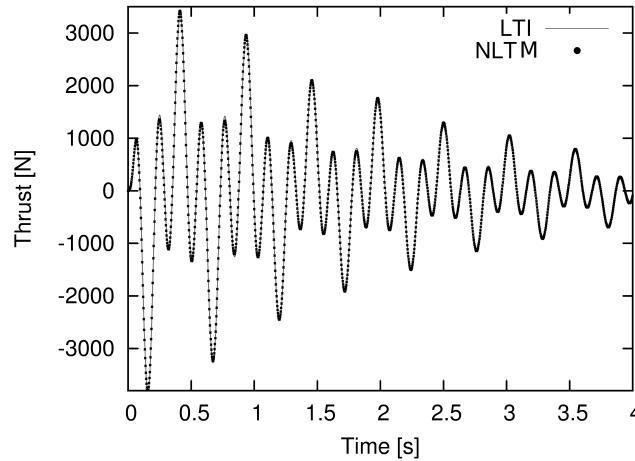


Figure 3.7.: Thrust due to collective pitch perturbations, hovering flight. LTI vs NLTM predictions.

3. Linear time invariant model extraction from high-fidelity solvers

For θ_{com} defined as:

$$\theta_{com} = A \sin(\omega t) \cos(2\omega t) e^{(-\alpha t)} \quad (3.40)$$

with $A = 0.01$ rad, $\omega = 0.3\Omega$ and $\alpha = 0.04\Omega$, and considering θ_{com} as perturbation to collective pitch (namely, $\theta_{com} \equiv \theta_0$), figure 3.7 shows the corresponding thrust perturbations predicted in hovering flight condition both by the high-fidelity NLTM solver and by the LTI model. The comparison demonstrates that the simulations provided by the proposed reduced-order formulation are very accurate. However, for hovering condition, under the assumption of null cyclic pitch, predictions are not affected by the time-constant approximation of the aeroelastic system, thus limiting the assessment to the linearization process and reduction to a finite number of state variables.

Unlike, in forward flight at $\mu = 0.3$, the aeroelastic response is affected by time-periodic effects. For this flight condition, figure 3.8a depicts the hub forces generated by lateral cyclic pitch perturbations (namely, $\theta_{com} \equiv \theta_c$) as predicted by both the NLTM solver and by the finite-state, LTI model. Similarly, in-plane hub moments due to collective pitch perturbations given by the two aeroelastic solution approaches are shown in figure 3.8b. Although concerning an advancing rotor, NLTM and LTI model responses are still in very good agreement.

It is worth reminding that, LTI-model and NLTM results presented in figure 3.8 concern loads perturbations with respect to the steady reference flight. Therefore, stationary and 4/rev components of loads arising in the unperturbed flight do not appear, in that they are cancelled-out in the first step of the aeroelastic transfer matrices extraction (see section 3.1.1). According to equation 3.40, figure 3.9 shows that the main spectral components of the perturbation responses in figure 3.8 are around frequencies ω and 3ω , with smaller multi-harmonic components due to the intrinsic periodicity of the aeroelastic operator (captured only by the NLTM solution), around frequencies $4\Omega - \omega, 4\Omega + \omega, 4\Omega - 3\omega, 4\Omega + 3\omega$ (see vertical solid lines). Further multi-harmonic components around 8Ω could appear, but in this case these are absolutely negligible. Specifically, figures 3.9a and 3.9a show, in addition to the input spectrum (bottom pictures), the spectra of the corresponding LTI and NLTM predictions of

3. Linear time invariant model extraction from high-fidelity solvers

longitudinal force, F_x and pitching moment, M_y , respectively. In these figures, the effects of the slightly damped lag modes (with frequencies identified by the vertical dashed lines) are also clearly observed both in LTI and in NLTM spectra: in particular, a progressive mode peak is present in figure 3.9a, whereas the response in figure 3.9b is significantly affected by a regressive mode peak. Except for the multi-harmonic components hidden to the LTI model (and not interesting for flight dynamics purposes), the comparisons between output spectra confirm the very good quality of the simulation provided by the proposed approach. In section 4 a methodology to capture also the multiharmonic effects neglected by the LTI model will be presented.

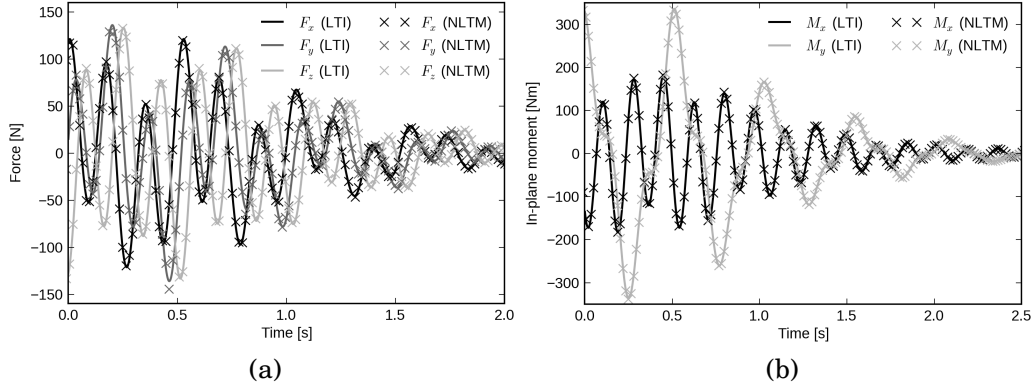


Figure 3.8.: Forward flight perturbed hub loads. LTI vs NLTM time response predictions.

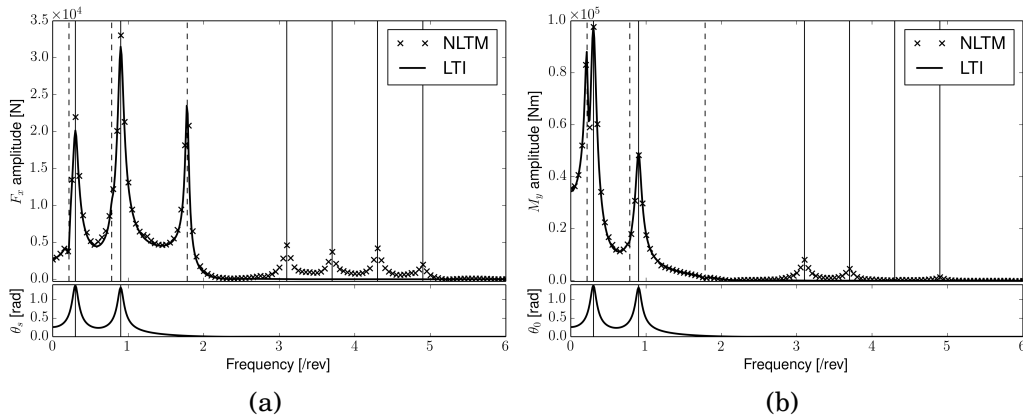


Figure 3.9.: Forward flight perturbed hub loads. Spectra of LTI and NLTM predictions.

3. Linear time invariant model extraction from high-fidelity solvers

Furthermore, the response to a non-oscillatory type of θ_{com} is examined. It consists of a (smoothed) 5.7-deg collective pitch step input. For $\mu = 0.3$, corresponding hub loads given by the high-fidelity NLTM solver and the LTI model are compared in figure 3.10. It shows that also in this case the two solutions perfectly match in terms of both transitory and asymptotic responses.

Thus, it is demonstrated that the finite-state, LTI model is a tool well suited for accurate, real-time prediction of rotor hub loads produced by airframe motion and blade pitch control perturbations.

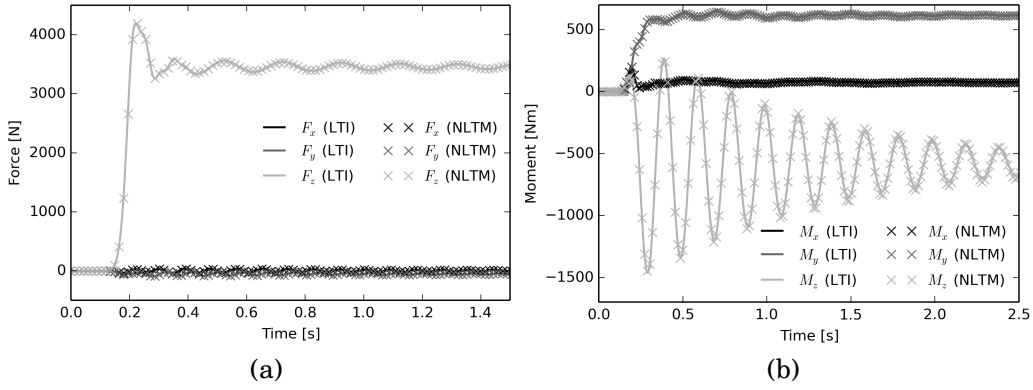


Figure 3.10.: Hub loads response to indicial collective pitch in advancing flight. LTI vs NLTM predictions.

3.3.3. Influence of the additional states dynamics

As shown in sections 3.1.1 and 3.1.2, the identification of the aeroelastic poles requires an usually non negligible computational effort. Moreover, for real time applications there is an hard limit to the number of internal states that can be used³. For high frequency inputs, in particular for input frequencies near to the system poles, a behavior dominated by the additional states dynamics is expected. However, for flight dynamics applications the range of frequencies of interest is limited, and usually it does not exceed 10 Hz. Therefore it may not be obvious to evaluate the importance of performing an accurate aeroelastic modeling for applications such as real time simulations.

³However true, as shown in section 6 this maximum number of poles is in the order of the hundreds even for consumer hardware.

3. Linear time invariant model extraction from high-fidelity solvers

Mode	Real part [1/s]	Imaginary part [rad/s]
I regressive flap	-14.5	3.93
I regressive lag	-0.97	9.46
actual lag mode	-0.95	35.0
II regressive flap	-17.3	42.1
actual flap mode	-15.3	48.4
II regressive flap	-0.96	53.8
I progressive lag	-0.97	79.3
I progressive flap	-13.9	92.5

Table 3.1.: Pole locus of the aeroelastic modes with a frequency less than 15 Hz

In this section an analysis of the importance of the additional states dynamics on the accuracy of the LTI rotor model for low frequency inputs is presented. To perform this analysis a rotor having quasi-steady aerodynamics and Pitt-Peters inflow model and using one flapping mode and one lag mode for the blade structural dynamics was considered. A LTI finite-state model was obtained for a trimmed flight at $\mu = 0.25$. In table 3.1 some of the eigenvalues of A , representing the poles of the aeroelastic modes are detailed. In section 3.3.1 it was pointed out that of the poles frequency is governed by the structural dynamics, while the aerodynamics has a greater influence on the poles damping. It is also worth noting that due to the periodic nature of the aerodynamics and of the input variables, the poles related to the structural modes are scattered by $\pm jn\Omega$, so they appear also for much lower frequencies than the actual structural eigenfrequency. For example the actual flap and lag aeroelastic modes have a frequency of 48 rad/s and 35 rad/s respectively, but their regressive modes have a frequency of about 4 rad/s and 9 rad/s , well inside the range of interest for flight simulation.

The resulting LTI was perturbed with nine quadratic chirp inputs of unitary amplitude (1 m/s for the velocities, 1 rad/s for the angular velocities and 1° for the blade pitch controls). Two different sets of outputs were then considered: the full LTI system output $\delta f(t)$, and the output $\delta f_s(t)$ of an LTI system lacking the internal dynamics, or in other words a system with an infinitely fast internal dynamics:

$$\delta f_s(t) = \mathbf{X}\delta \mathbf{u}(t) + \mathbf{D}_1\delta \dot{\mathbf{u}}(t) + \mathbf{D}_2\delta \ddot{\mathbf{u}}(t) \quad (3.41)$$

3. Linear time invariant model extraction from high-fidelity solvers

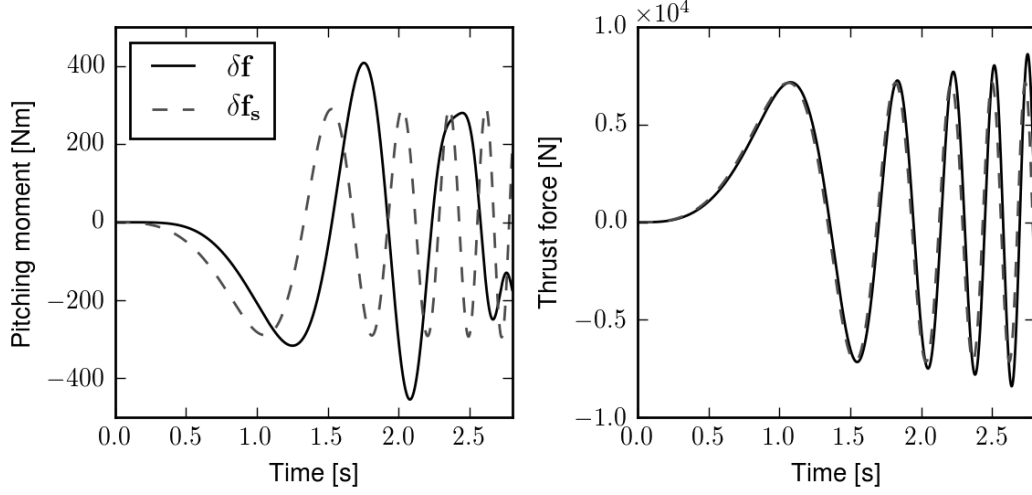


Figure 3.11.: Comparison of outputs δf and δf_s . Pitching moment M_y vs a horizontal velocity perturbation U (left), and vertical force F_z vs collective pitch perturbation θ_0 (right).

where X is the static derivatives matrix, defined in equation 3.38. In figure 3.11 these outputs are depicted for two particular cases. In figure 3.11a the pitching moment M_y caused by an horizontal velocity perturbation U is shown. In this case there is a substantial difference between the two outputs. On the contrary, in figure 3.11b, depicting the vertical force caused by a collective input, the dynamic of the additional states has a small effect on the total accuracy. The reason for this difference resides in the modes governing the two outputs and in their characteristic frequency.

To summarize the importance of the additional states dynamics for all the 54 input/output combinations the median of the following normalized index was employed:

$$\mathcal{K}(t) = \frac{|\delta f(t) - \delta f_s(t)|}{\delta f(t)} \quad (3.42)$$

and presented in figure 3.12. Of course when the influence of the additional states dynamics is negligible, a null, or small $\tilde{\mathcal{K}}$ is obtained. On the contrary, when the phenomenon is governed by the internal dynamics, a $\tilde{\mathcal{K}}$ with an order of magnitude of one is expected.

From figure 3.12 it is possible to see that most input/output dynamics are heavily influenced by the additional states dynamics, even in the limited frequency range considered here, confirming the importance of

3. Linear time invariant model extraction from high-fidelity solvers

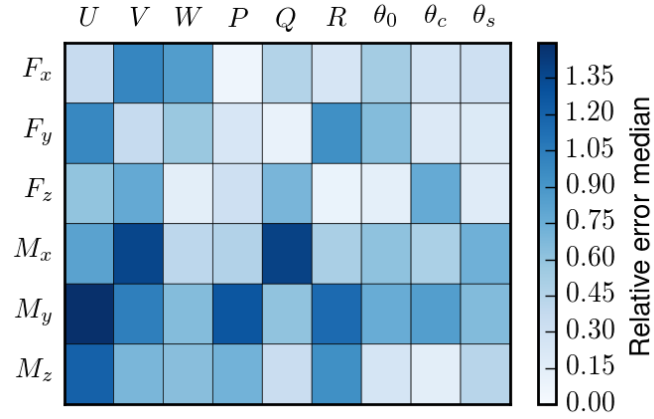


Figure 3.12.: Heatmap of the median relative error committed by neglecting the additional states dynamics for a low frequency input.

modeling the aeroelastic behavior of the rotor even for flight simulation tasks.

4. Linear time periodic model extraction from high-fidelity solvers

4.1. Introduction to harmonic transfer function

The ability of taking into account the intrinsic periodic nature of the physics of helicopter rotors arises in many applications and is an essential feature of an identification framework. In particular, even if for some application the time-periodic behavior of a phenomenon can be neglected, in others it represents an essential feature. For the aeroelastic operator studied in this work the importance of the time-periodic behavior depends on the application. In section 6 it will be shown that for general flight simulation tasks a time invariant approximation is good enough. However for other applications, such as the analysis of the helicopter with the rotor coupled with the fuselage structural modes [BSCG13], it may be important having a state space model capable of describing the higher frequency output caused by an arbitrary input. Moreover, in the previous section the limits of the chirp excitation method for non-parametric identification were highlighted: when applied to time periodic systems this methodology suffers from a loss of accuracy.

In this section the extension of the non-parametric identification methodology to linear time periodic systems will be presented.

The general form of a linear time periodic (LTP) dynamical systems is similar to the classical LTI system equation, with the notable difference

4. Linear time periodic model extraction from high-fidelity solvers

of the time periodicity of the involved matrices:

$$\begin{aligned}\mathbf{f} &= \mathbf{C}(\psi) \mathbf{r} + \mathbf{D}(\psi) \mathbf{u} \\ \dot{\mathbf{r}} &= \mathbf{A}(\psi) \mathbf{r} + \mathbf{B}(\psi) \mathbf{u}\end{aligned}\tag{4.1}$$

where $\psi = \Omega_p t$. The matrices defining the realization in 4.1 are defined as a series of harmonic components with base frequency Ω_p . For example matrix $\mathbf{A}(t)$ can be defined as:

$$\mathbf{A}(t) = \mathbf{A}_0 + \sum_{k=1}^{\infty} (\mathbf{A}_k e^{jk\Omega_p t} + \mathbf{A}_{-k} e^{-jk\Omega_p t})\tag{4.2}$$

and the same can be done for matrices $\mathbf{B}(t)$, $\mathbf{C}(t)$ and $\mathbf{D}(t)$.

The fundamental difference between a LTI system and a linear time periodic (LTP) system is that the transfer function of the former maps a sinusoidal input signal at a given frequency into a sinusoidal output signal at the same frequency, possibly with different amplitude and phase. In contrast, the latter maps a sinusoidal input signal to a periodic output signal composed by an infinite number of harmonics, each with different gains and phases¹.

This one-to-many behavior of the harmonics can not be described by a transfer function as defined for linear time invariant systems, but a different definition of transfer function is needed. This definition was introduced in [WH90] and it is at the base of the harmonic balance technique. The harmonic transfer function \mathbf{H} (HTF) relates the harmonics of the input signal \mathbf{u} to the harmonics of the output signal \mathbf{y} :

$$\tilde{\mathbf{y}}(s) = \mathbf{H}(s) \tilde{\mathbf{u}}(s) \quad \left\{ \begin{array}{c} \vdots \\ \tilde{\mathbf{y}}_{-1}(s) \\ \tilde{\mathbf{y}}_0(s) \\ \tilde{\mathbf{y}}_1(s) \\ \vdots \end{array} \right\} = \mathbf{H}(s) \left\{ \begin{array}{c} \vdots \\ \tilde{\mathbf{u}}_{-1}(s) \\ \tilde{\mathbf{u}}_0(s) \\ \tilde{\mathbf{u}}_1(s) \\ \vdots \end{array} \right\}\tag{4.3}$$

where the input and output vectors are defined in the time domain as a

¹A good bibliography on this topic can be found in [LPL14].

4. Linear time periodic model extraction from high-fidelity solvers

series of modulated signals:

$$\begin{aligned} \mathbf{y}(t) &= \mathbf{y}_0(t) + \sum_{k=1}^{\infty} (\mathbf{y}_k(t) e^{jk\Omega_p t} + \mathbf{y}_{-k}(t) e^{-jk\Omega_p t}), \\ \mathbf{u}(t) &= \mathbf{u}_0(t) + \sum_{k=1}^{\infty} (\mathbf{u}_k(t) e^{jk\Omega_p t} + \mathbf{u}_{-k}(t) e^{-jk\Omega_p t}), \end{aligned} \quad (4.4)$$

where Ω_p is again the base periodicity of the system. A similar decomposition can be applied to the harmonic transfer function matrix $\mathbf{H}(s)$, leading to a block matrix representation:

$$\mathbf{H}(s) = \begin{bmatrix} \ddots & \vdots & \vdots & \vdots & \ddots \\ \cdots & \mathbf{H}_{-1-1}(s) & \mathbf{H}_{-10}(s) & \mathbf{H}_{-11}(s) & \cdots \\ \cdots & \mathbf{H}_{0-1}(s) & \mathbf{H}_{00}(s) & \mathbf{H}_{01}(s) & \cdots \\ \cdots & \mathbf{H}_{1-1}(s) & \mathbf{H}_{10}(s) & \mathbf{H}_{11}(s) & \cdots \\ \ddots & \vdots & \vdots & \vdots & \ddots \end{bmatrix}. \quad (4.5)$$

Each block of \mathbf{H} is a LTI transfer function matrix relating a component of the output with a component of the input:

$$\tilde{\mathbf{y}}_k(s) = \mathbf{H}_{kj}(s) \tilde{\mathbf{u}}_j(s) \quad (4.6)$$

The harmonic transfer function matrix $\mathbf{H}(s)$ is theoretically a doubly infinite matrix. However, for obvious reasons, said matrix is truncated and only the contribute of a finite number of harmonics n_h is included.

It is worth noting that said components of \mathbf{y} and \mathbf{u} , as defined in equation 4.4, are actually time signals themselves. This means that there are infinite possible decompositions of any signal. For example, an input signal $\mathbf{u}(t)$ can be decomposed using a Fourier series, thus obtaining a possibly infinite number of constant components \mathbf{u}_k ; alternatively the same signal can be decomposed using only a limited number of components, or even only one component (e.g. $\mathbf{u}_0(t) = \mathbf{u}(t)$). Once the decomposition of the input is defined the components of the output $\mathbf{y}_k(t)$ are obtained by the application of equation 4.6. Theoretically, if an infinite harmonic transfer function matrix is considered the choice of the decomposition of \mathbf{u} and \mathbf{y} does not influence the resulting input/output relation. However

4. Linear time periodic model extraction from high-fidelity solvers

due to the finiteness of \mathbf{H} , the input signal has to be decomposed using only $m = n_h + 1$ components.

Another important aspect of $\mathbf{H}(s)$, highlighted by the arbitrariness of the input decomposition, is that it is possible to completely define any block-diagonal of $\mathbf{H}(s)$ from a single block element $\mathbf{H}_{kl}(s)$ of said diagonal:

$$\mathbf{H}_{kl}(j\omega + n\Omega_p) = \mathbf{H}_{k+n, l+n}(j\omega). \quad (4.7)$$

In other words it is possible to define the full matrix $\mathbf{H}(s)$ by defining just one row or one column of blocks. Finally, when the HTF matrix describes a real system the following property is also valid:

$$\mathbf{H}_{k,l}(j\omega) = \mathbf{H}_{k,-l}^*(-j\omega) \quad (4.8)$$

In this work all the systems analyzed are real, so it is convenient to introduce a transformation of $\mathbf{H}(s)$ such that the input and output signals are defined in terms of sinusoidal components instead of complex exponential components:

$$\begin{aligned} \mathbf{y}(t) &= \mathbf{y}_0(t) + \sum_{k=1}^{\infty} [\mathbf{y}_{kc}(t) \cos(k\Omega_p t) + \mathbf{y}_{ks}(t) \sin(k\Omega_p t)], \\ \mathbf{u}(t) &= \mathbf{u}_0(t) + \sum_{k=1}^{\infty} [\mathbf{u}_{kc}(t) \cos(k\Omega_p t) + \mathbf{u}_{ks}(t) \sin(k\Omega_p t)]. \end{aligned} \quad (4.9)$$

This can be achieved by employing the following equivalence, obtained by applying Euler formula:

$$\mathbf{y}_{kc} = \mathbf{y}_{-k} + \mathbf{y}_k \quad \mathbf{y}_{ks} = i(\mathbf{y}_k - \mathbf{y}_{-k}) \quad (4.10)$$

A transformation matrix \mathbf{T} describing this change of coordinates can be

4. Linear time periodic model extraction from high-fidelity solvers

defined accordingly:

$$\begin{pmatrix} \mathbf{y}_0 \\ \mathbf{y}_{1c} \\ \mathbf{y}_{1s} \\ \vdots \end{pmatrix} = \mathbf{T} \begin{pmatrix} \vdots \\ \mathbf{y}_{-1} \\ \mathbf{y}_0 \\ \mathbf{y}_1 \\ \vdots \end{pmatrix} \quad \begin{pmatrix} \mathbf{u}_0 \\ \mathbf{u}_{1c} \\ \mathbf{u}_{1s} \\ \vdots \end{pmatrix} = \mathbf{T} \begin{pmatrix} \vdots \\ \mathbf{u}_{-1} \\ \mathbf{u}_0 \\ \mathbf{u}_1 \\ \vdots \end{pmatrix} \quad (4.11)$$

and a HTF matrix $\mathbf{G}(s)$, similar to $\mathbf{H}(s)$ but relating sinusoidal components of input/output instead of complex exponential components, can be defined as:

$$\mathbf{G}(s) = \mathbf{T}\mathbf{H}(s)\mathbf{T}^{-1} \quad (4.12)$$

The main advantage of using $\mathbf{G}(s)$ in place of $\mathbf{H}(s)$ is that the former is a transfer function matrix describing a real LTI system, while the latter, for the properties of equation 4.7, is a transfer function matrix describing a complex LTI system. As such, once the non-parametric identification of $\mathbf{G}(s)$ is carried out, using one of the approaches described in the next section, it is possible to treat the problem as a normal real valued LTI system for the parametric identification, hence using the same tools developed in section 3.2 for LTI systems to obtain a state space representation.

4.2. Linear time periodic transfer function extraction

In this section the theory regarding LTP systems and the harmonic transfer function (HTF) matrix representation presented above will be used to develop a method for the non-parametric identification of the HTF matrix of the aeroelastic operator under consideration in this work. This is an extension of that introduced in section 3.1.2 for the identification of LTI systems.

4.2.1. **Extension of the chirp excitation method to LTP systems**

In section 3.1.2 a procedure for the identification of LTI systems using an input signal having a band spectrum (chirp) was presented. Using this procedure it is possible to extract the transfer functions for the frequencies comprised inside this band by using a single perturbation for each input. It was also highlighted that this methodology suffers from an accuracy loss when applied to time-periodic systems. The reason for this limitation is due to the fact that there is no way to distinguish if an harmonic component of the output, having a frequency inside band spectrum of the input signal, is the result of the response of a LTI system excited at the same frequency or is the result of a time periodicity of the system. Even the coherence, defined in equation 3.5, is not able to give an indication of that. For this reason, more information than those given by a single perturbation of the system are needed to carry out a correct LTI identification, and to perform an harmonic transfer function identification.

An important characteristic of LTP systems, highlighted in the previous section, is that the output signal depends not only on the input signal, but also on the phase of the input signal with respect to the internal system phase ψ . In [Sid01, SCH05] an identification methodology exploiting this characteristic was presented: the idea is to apply the same input to the LTP system multiple times, with different delays T with respect to the beginning of a system period. By properly analyzing the various outputs it becomes possible to differentiate between the effects of the various harmonic transfer functions (HTF). Two approaches are proposed in [Sid01] for the actual identification of the HTF: a first approach employing the discrete Fourier transformation, suffering from all the noise related issues described in section 3.1.2, and a second approach using an ill defined power/cross spectral density along with an heuristic assumption on smoothness of the transfer functions. These two approaches, especially the second, were both found unable to properly identify the LTP aerodynamic and aeroelastic rotor operators under analysis with a sufficient accuracy. For this reason an alternative approach is hereby presented.

4. Linear time periodic model extraction from high-fidelity solvers

Recalling the definition of the HTF given in section 4, it is possible to write the output of a LTP system excited by an input $\mathbf{u}(t)$ as:

$$\mathbf{y}(t, T) = \mathbf{y}_0(t) + \sum_{k=1}^{\infty} [\mathbf{y}_{kc}(t) \cos(k\Omega_p(t+T)) + \mathbf{y}_{ks}(t) \sin(k\Omega(t+T))]. \quad (4.13)$$

This equation is equivalent to equation 4.9, the only difference being the explication of the dependency of the output on the delay T . The Laplace transform of each of the output components \mathbf{y}_{kc} , \mathbf{y}_{ks} is in turn given by equation 4.6. If the input is considered as formed by only one component:

$$\mathbf{u}(t) = \mathbf{u}_0(t) \quad (4.14)$$

it becomes possible to express the components of the output in the Laplace domain as:

$$\mathbf{y}_0(s) = \mathbf{G}_{0,0} \mathbf{u}_0(s), \quad \mathbf{y}_{kc}(s) = \mathbf{G}_{kc,0}(s) \mathbf{u}_0(s), \quad \mathbf{y}_{ks}(s) = \mathbf{G}_{ks,0}(s) \mathbf{u}_0(s). \quad (4.15)$$

or, in other words, by multiplying a block-column of the HTF matrix $\mathbf{G}(s)$ by the Laplace transform of the input signal $\mathbf{u}_0(s)$. As described in section 4, the blocks of $\mathbf{G}(s)$ can be considered as transfer functions of a real valued LTI dynamical system. Then, if the signals $\mathbf{y}_0(t)$, $\mathbf{y}_{kc}(t)$, $\mathbf{y}_{ks}(t)$ can be isolated, it would be possible to apply the methodology developed in 3.1.2 for identifying the HTF blocks $\mathbf{G}_{0,0}(j\omega)$, $\mathbf{G}_{kc,0}(j\omega)$, $\mathbf{G}_{ks,0}(j\omega)$.

The decomposition of the output signal, described in equation 4.13, can be carried out in the time domain or in the frequency domain. The former approach is employed here.

The system is perturbed with the same chirp signal but using N_T different delays T_i and the various outputs $\mathbf{y}(t, T_i)$ are recorded. Then, for

4. Linear time periodic model extraction from high-fidelity solvers

every time step the following linear system is solved²:

$$\mathbf{R}(t) \begin{bmatrix} \mathbf{y}_0(t) \\ \mathbf{y}_{1c}(t) \\ \mathbf{y}_{1s}(t) \\ \vdots \\ \mathbf{y}_{n_h c}(t) \\ \mathbf{y}_{n_h s}(t) \end{bmatrix} = \begin{bmatrix} \mathbf{y}(t, T_1) \\ \mathbf{y}(t, T_2) \\ \mathbf{y}(t, T_3) \\ \vdots \\ \mathbf{y}(t, T_{N_T}) \end{bmatrix} \quad (4.16)$$

and the output components are identified. The matrix $\mathbf{R}(t)$ is defined as:

$$\mathbf{R}(t) = \begin{bmatrix} 1 & \cos(\Omega_p(t+T_1)) & \sin(\Omega_p(t+T_1)) & \cdots & \cos(n_h\Omega_p(t+T_1)) & \sin(n_h\Omega_p(t+T_1)) \\ 1 & \cos(\Omega_p(t+T_2)) & \sin(\Omega_p(t+T_2)) & \cdots & \cos(n_h\Omega_p(t+T_2)) & \sin(n_h\Omega_p(t+T_2)) \\ 1 & \cos(\Omega_p(t+T_3)) & \sin(\Omega_p(t+T_3)) & \cdots & \cos(n_h\Omega_p(t+T_3)) & \sin(n_h\Omega_p(t+T_3)) \\ \vdots & \vdots & \vdots & \ddots & \vdots & \vdots \\ 1 & \cos(\Omega_p(t+T_{N_T})) & \sin(\Omega_p(t+T_{N_T})) & \cdots & \cos(n_h\Omega_p(t+T_{N_T})) & \sin(n_h\Omega_p(t+T_{N_T})) \end{bmatrix}.$$

The number of input perturbations N_T should be greater or equal than the number of components sought in the identification:

$$N_T \geq 2n_h + 1 \quad (4.17)$$

where n_h are the number of harmonics considered.

4.3. Numerical results

4.3.1. Aerodynamic model

In this section some results regarding a purely aerodynamic model are presented. In terms of input and outputs this model is analogous to the aeroelastic model used throughout this work, but it lacks the internal structural degrees of freedom: the rotor blades are in fact considered rigid. In this case the additional states represent only the aerodynamic poles. This aerodynamic model is similar to that introduced in [GM12] and it is extended here to consider an arbitrary number of input/output harmonics.

²The columns of the matrix $\mathbf{R}(t)$ are orthogonal to each other so an efficient solution of the system is possible.

4. Linear time periodic model extraction from high-fidelity solvers

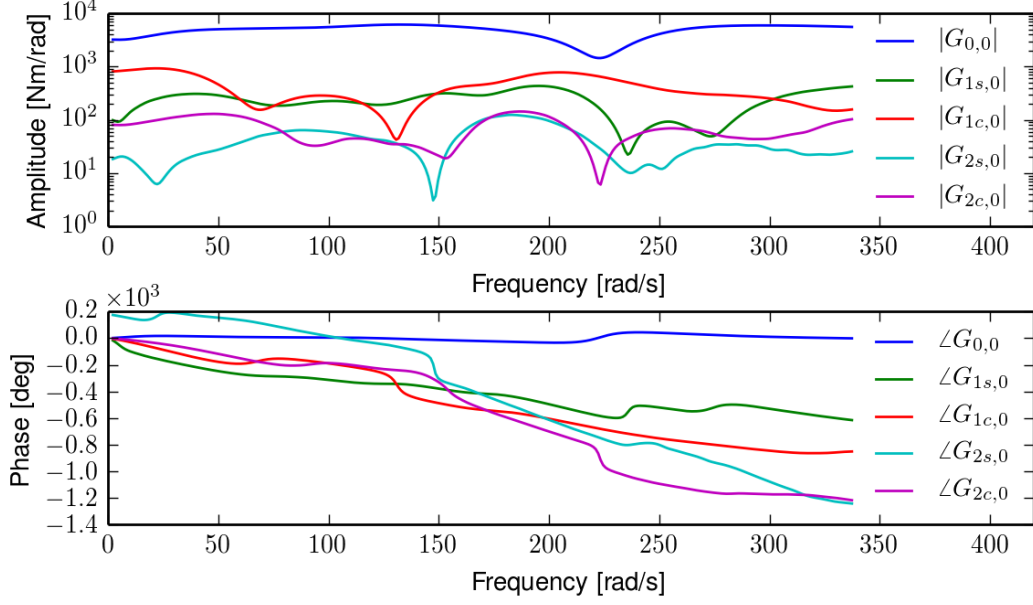


Figure 4.1.: Harmonic transfer functions relating the rolling moment with the collective pitch input.

The aerodynamic predictions used to extract the aerodynamic forces model are obtained by an unsteady, potential-flow, boundary element method (BEM) tool for rotorcraft, extensively validated in the past [GB07].

A Bo-105 type rotor with an advancing ratio $\mu = 0.2$ was analyzed. The LTP chirp methodology described in section 4.2.1 was employed to extract the harmonic transfer function (HTF) matrix of the aerodynamic operator having periodicity equal to:

$$\Omega_p = 4\Omega \quad (4.18)$$

where $\Omega = 44.4 \text{ rad/s}$ is the rotor angular speed.

Five different delays were considered to extract five blocks of the HTF matrix $G(s)$ up to a frequency of 8Ω . This is a 30×9 matrix containing five 6×9 blocks. For sake of conciseness only a specific transfer function is here analyzed, in particular the transfer function relating the rolling moment M_x with the collective pitch control θ_0 . This function was chosen as a good example where a time periodic model is able to improve the accuracy considerably. The five harmonic transfer functions are depicted in figure 4.1 as absolute value and phase.

4. Linear time periodic model extraction from high-fidelity solvers

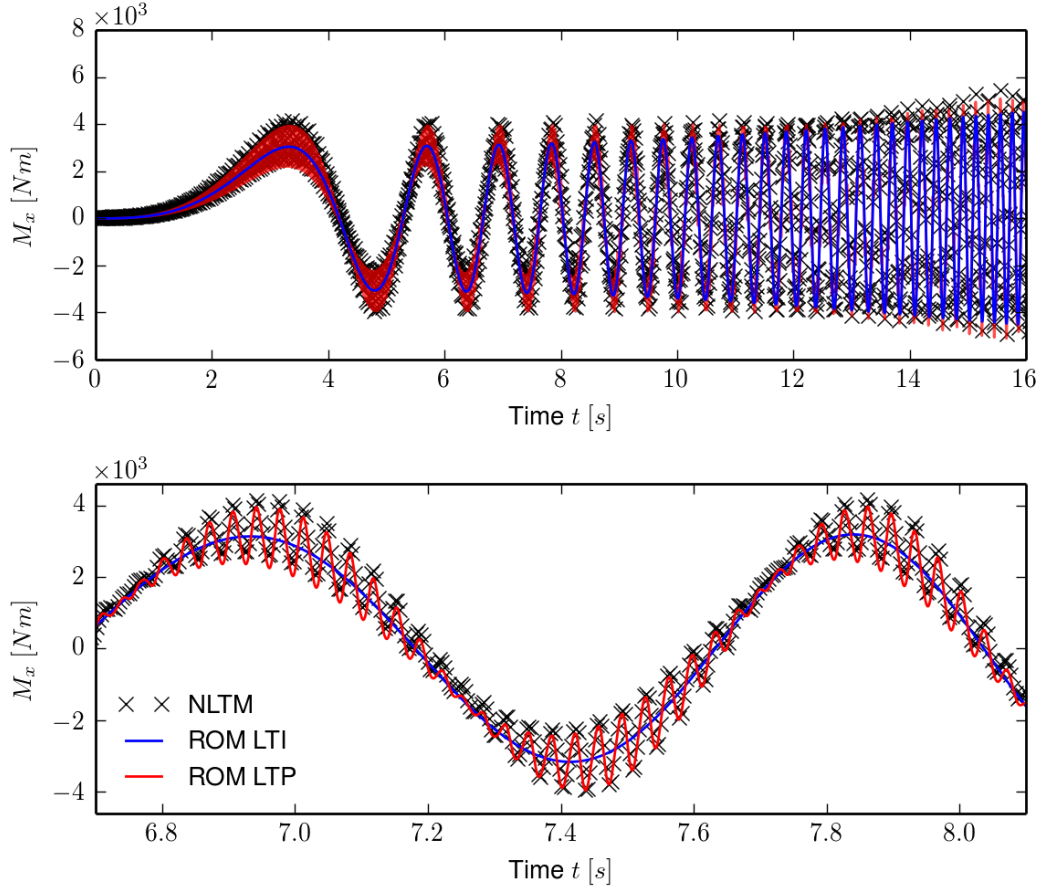


Figure 4.2.: Time-marching response of the aerodynamic rolling moment to a collective pitch chirp input, spanning from 0 to 70 rad/s. The complete signals (top) and a zoomed view (bottom)

A rational matrix approximation of these transfer functions, along with the other 265 not shown here, was calculated using the methodology explained in section 3.2, and a state space model analogous to that of equation 2.10 was obtained. To validate this model it was perturbed with a collective pitch chirp input with one degree of amplitude, spanning from 0 to 70 rad/s, and the measured obtained was compared to the nonlinear time-marching (NLTM) solution given by the BEM solver when perturbed with the same input. The output obtained by a LTI model was also compared to show the differences of accuracy in the two models. Figure 4.2 shows this comparison: the greater accuracy of the LTP model with respect to the LTI model is noticeable, in particular for a low frequency input the high frequency component of the output, related to the time-periodicity of the system, is not negligible. In figure

4. Linear time periodic model extraction from high-fidelity solvers

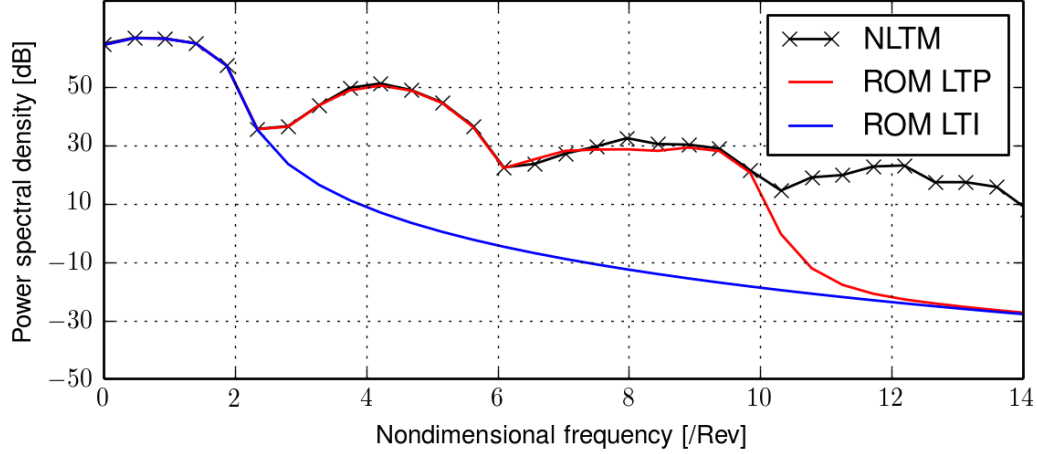


Figure 4.3.: Power spectral density of the time-marching response of the aerodynamic rolling moment to a collective pitch chirp input, spanning from 0 to 70 rad/s..

4.3 the power spectral density of these signals is shown. The output of the nonlinear, time-periodic solver is characterized by a series of bands, about 140 rad/s wide, shifted by $\Omega_p = 4\Omega$ by the time periodicity of the operator. While the LTI model is able to model just the first band, the LTP model employed here, identified using $n_h = 2$ harmonics is able to correctly capture also the second and the third bands, centered around 4Ω and 8Ω .

The importance of being able to model the time periodicity of the aerodynamic operator resides in the following considerations: high-fidelity aerodynamic solvers have usually very high computational costs. Due to the slightly damped dynamic of the blades, to perform an accurate identification of the aeroelastic operator, long simulations are required (see both 3.1.1 and 3.1.2). On the other hand aerodynamic poles are more damped, and as such it may be computationally cheaper to obtain an aerodynamic state-space model, even considering the LTP identification overheads, and coupling it to the structural operator successively, than obtaining the aeroelastic operator through a coupled solver (as it was done in this work, see 3.3), especially if strong coupling is needed. Moreover an alternative approach may be employed to efficiently obtain aeroelastic operators: recently the author and others presented an aerodynamic state-space model describing the dynamic of the wake inflow for

4. *Linear time periodic model extraction from high-fidelity solvers*

conventional [GGS⁺15, GGS⁺16] and unconventional rotors [CGB⁺15]. In particular in [GGS⁺16] it was observed that a time periodic modeling is essential to correctly capture the inflow effects.

4.3.2. Aeroelastic model

Below some results regarding the application of the LTP extraction methodology to an aeroelastic solver are presented. A trimmed forward flight condition with $\mu = 0.3$, regarding the usual Bo-105 rotor, was considered.

5. Model stitching

In this section the topic of model stitching for obtaining the helicopter rotor model described in section 2.2.3 and valid in the entire flight envelope will be addressed.

The term model stitching was introduced in [DPA⁺07, ZT10] and refers to the process of combining discrete state-space perturbation models and the associated trim data into a single continuous full-envelope flight-dynamics simulation model. The model stitching technique employed in [ZT10][TTBH15] is however different from that developed for this work, both in terms of computational procedure and time domain application. The approach presented here is in fact more general and can be applied to black box solvers, while a certain knowledge of the dynamics of the identified systems is required to apply the technique of [ZT10].

The base idea, as explained in 2.2.3, is to identify a set of parameters ζ (for example the advancing ratio and the shaft angle of attack) affecting the helicopter dynamic response and to apply the identification procedures explained in section 3 to obtain a series of transfer functions of the perturbation dynamics for several flight conditions described by ζ . While in [ZT10] a gray box parametric identification is carried out for each one of transfer functions and then the matrices A , B , C and D_0 are interpolated, it is not possible to do the same when a generic parametrization is employed. In this case accurate and regular interpolation of differential models is not a straightforward task. As detailed in section 3.2.1, when a non-injective parametrization of C , A and B is employed it is not possible to interpolate the coefficients of these matrices, as they not necessarily have the same meaning in the different identifications. On the other hand even by employing a general injective parametrization, as numerical tests have confirmed, there is no guarantee that the coefficients will have a regular variation.

5. Model stitching

To obtain a regular interpolation of the state-space matrices, leading to a valid description of the dynamic in the full flight envelope, matrices D_2 , D_1 , D_0 , C , A , B are identified following a procedure specifically developed to guarantee a smooth variation of model matrices within the range of operating condition considered. To obtain this the additional degrees of freedom introduced by ζ are optimized in a procedure similar to that described in section 3.2.2.

Akin to the previously described modeling procedures, the first step of the procedure consists in extracting the frequency-response functions $E(s, \zeta)$ by perturbing the high-fidelity time-marching aeroelastic solver for a given set of operating conditions within the flight envelope of interest. Then the the following optimization problem is formulated:

$$\min \sum_{i,j}^{N_f, N_s} \|\mathbf{Q}(\jmath\omega_i, \zeta_j)\|^2 \quad (5.1)$$

where the residual matrix \mathbf{Q} , similarly to equation 3.32, is defined as:

$$\mathbf{Q}(\jmath\omega, \zeta) = -\omega^2 \mathbf{D}_2(\zeta) + \jmath\omega \mathbf{D}_1(\zeta) + \mathbf{D}_0(\zeta) + \mathbf{C}(\zeta) [\jmath\omega \mathbf{I} - \mathbf{A}(\zeta)]^{-1} \mathbf{B}(\zeta) - \mathbf{E}(\jmath\omega, \zeta), \quad (5.2)$$

while the summation is up to the number of sampled frequencies N_f and the number N_s of flight conditions considered. The dependency of all the state-space matrices on the vector ζ is analytically approximated through linear combinations of b-spline functions [PT12]. The advantage in using these interpolating functions lies in the possibility of adopting optimal sets of input data locations in the space of parameters, that allow best fitting of matrix coefficients variation. For instance, in our kind problems, input data are conveniently concentrated near hovering flight condition, where the gradient of transfer functions is expected to be relevant. The coefficients of b-splines combinations expressing matrix entries are the variables to be identified by solving of the optimization problem.

It is important to note that to guarantee the smoothness of the solution, a fundamental condition to be satisfied to obtain accurate model interpolations is that the number of variables of the unique problem is strictly less than the sum of the number of variables of single approximations

5. Model stitching

that would be introduced in the sequential interpolation problem. If this condition were not met, then the optimal solution of the unique problem would coincide with the solution given by the sequential solver. Reducing the variables space is a mean to impose a smooth variation of the coefficients and solving the issues related to the not injectivity of the single identifications.

Of course, the solution of an optimization problem comprising all interpolation variables at the same time poses a bigger numerical challenge, with respect to solving a set of separate smaller interpolation problems. For this reason the same approach of separating the linear and the non-linear variables presented in section 3.2.2 is employed, along with a set of gradient based optimizers as BFGS, SLSQP, CG [Joh14].

5.1. Application of the stitched model in the time domain

With the procedure described in the previous sections the coefficients defining the state-space matrices in the parameter space have been defined. These matrices represent the linear approximation of the underlying model behavior, valid in the neighborhood of the conditions defined by the parameter vector ζ . This approximation represents the dynamics of the system when it is perturbed with an input $\delta \mathbf{u} = \mathbf{u} - \mathbf{u}_0(\zeta)$ with respect to a reference input value \mathbf{u}_0 that depends on the parameter vector ζ . The reference input has to be chosen to minimize $\delta \mathbf{u}$ during the application of the model, hence limiting the approximations introduced by its linear nature. In this work, $\mathbf{u}_0(\zeta)$ was chosen by trimming the helicopter for a series of flight conditions depending on ζ , as detailed in section 6.

As previously shown, for a given ζ , the differential form of the LTI system in the time domain is the following:

$$\begin{aligned} \mathbf{f} &= \mathbf{f}_0(\zeta) + \mathbf{D}_0(\zeta) \delta \mathbf{u}(\zeta) + \mathbf{D}_1(\zeta) \delta \dot{\mathbf{u}} + \mathbf{D}_2(\zeta) \delta \ddot{\mathbf{u}} + \mathbf{C}(\zeta) \mathbf{r} \\ \dot{\mathbf{r}} &= \mathbf{A}(\zeta) \mathbf{r} + \mathbf{B}(\zeta) \delta \mathbf{u}(\zeta) \end{aligned} \quad (5.3)$$

where $\mathbf{f}_0(\zeta)$ is the reference output, also depending on ζ , defined as the

5. Model stitching

steady-state output of the system when a constant input $u_0(\zeta)$ is applied to it. While equation 5.3 is valid for a fixed ζ , in general it can not be used when the parameter vector depends on the time. To see why said equation may fail to correctly approximate the dynamics, it is sufficient to consider a maneuver in which the input vector u stays equal to $u_0(\zeta)$, thus leading to a null $\delta u(\zeta)$ perturbation input along the maneuver. In this case it is easy to see that the differential part of equation 5.3, the additional states dynamics, is never forced and does not contribute to the computed force. Indeed the only case where equation holds is when the same reference input $u_0(\zeta) = \bar{u}_0$ is used in the entire parameter space (hence the reference input vector does not depends on ζ). However, as it will be also shown in the following sections, having a single reference input vector is usually not convenient and sometime it is not possible. Moreover if ζ depends on u , hence a model that is nonlinear with respect to an input variable is sought, it means that $u_0(\zeta)$ depends in turn from ζ , invalidating the aforementioned assumption.

To employ the stitched model another differential form has to be used. In [GGP⁺15] the author, and others, proposed a solution based on the definition of the asymptotic steady state solution of the additional states dynamics; good results were obtained but later it was observed a loss of accuracy caused by numerical cancellations error. In this work an improved form, leading to a more stable numerical behavior is proposed. This form is based on the notion that the canonical LTI state space system equation:

$$\begin{aligned} y &= Cr + D_0 u + D_1 \dot{u} + D_2 \ddot{u} \\ \dot{r} &= Ar + Bu \end{aligned} \tag{5.4}$$

can be rewritten as:

$$\begin{aligned} y &= \hat{C} \dot{r} + \hat{D}_0 u + D_1 \dot{u} + D_2 \ddot{u} \\ \dot{r} &= Ar + Bu \end{aligned} \tag{5.5}$$

where \hat{C} and \hat{D}_0 are defined as:

$$\hat{C} = CA^{-1}, \quad \hat{D}_0 = D_0 - CA^{-1}B. \tag{5.6}$$

5. Model stitching

In particular it is worth noting that $\hat{\mathbf{D}}_0$ is the matrix of the static derivatives of the system \mathbf{X} introduced in 3.2.3 and, as such, it may be obtained directly from the interpolation of the various derivatives matrices instead. For a demonstration of the equivalence of the two differential forms please refer to appendix A.

The advantage of using equation 5.5 instead of equation 5.4 lays in the clear division of the output in two components: one depending algebraically on the input and one, the differential part, that is non-null only during the additional states transient.

Equation 5.5 is then extended for the application to the stitched model considering as:

$$\begin{aligned}\mathbf{f} &= \mathbf{f}_0(\zeta) + \hat{\mathbf{D}}_0(\zeta) \delta \mathbf{u}(\zeta) + \mathbf{D}_1(\zeta) \delta \dot{\mathbf{u}} + \mathbf{D}_2(\zeta) \delta \ddot{\mathbf{u}} + \hat{\mathbf{C}}(\zeta) \dot{\mathbf{r}} \\ \dot{\mathbf{r}} &= \mathbf{A}(\zeta) \mathbf{r} + \mathbf{B}(\zeta) \mathbf{u}(\zeta)\end{aligned}\tag{5.7}$$

In this way the additional states dynamics is forced by the full input \mathbf{u} instead of being forced by $\delta \mathbf{u}$.

5.2. Numerical results

The numerical investigation presented in this section has two main objectives: the validation of stitched rotor aeroelastic model proposed and the examination of its capability to predict loads transmitted to the airframe by a helicopter main rotor during maneuvers.

5.2.1. Validation of the identification process

First, the accuracy of the presented methodology in identifying the LTI, finite-state, main rotor representation for operational conditions included in the considered flight parameters domain is examined. Figure 5.1 presents examples concerning the effect of flight parameters, the advancing speed V and the shaft angle of attack α_{sh} , on aeroelastic transfer functions amplitude. In particular, in figure 5.1a it is shown the amplitude of the transfer function relating thrust force to pitching angular velocity, for three different flight speeds, whereas figure 5.1b depicts the

5. Model stitching

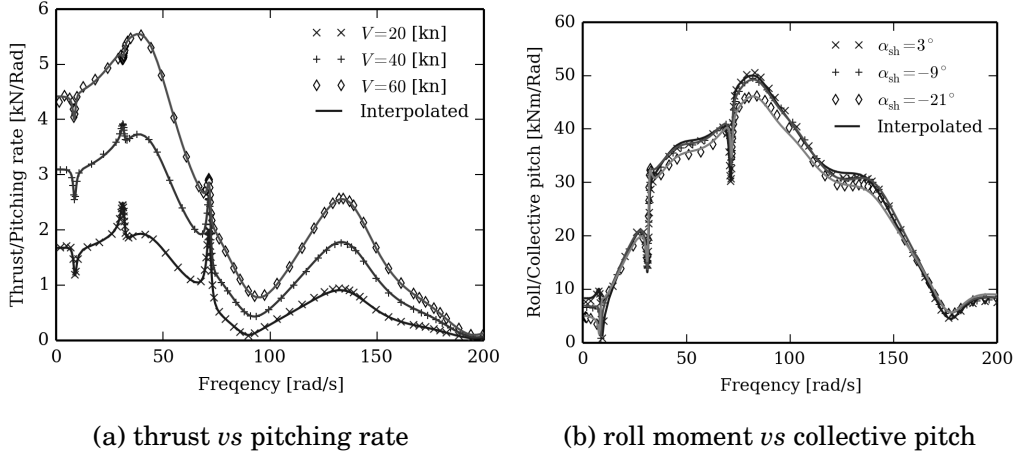


Figure 5.1.: Transfer functions variation with respect to forward velocity and shaft angle. Sampled vs interpolated amplitude frequency distribution.

amplitude of the transfer function relating rolling moment to blade collective pitch control, for three values of the rotor shaft angle of attack. For all examined cases, the results obtained by ROM solutions are compared with those directly identified through the aeroelastic numerical tool. These results reveal that the considered transfer functions present a remarkable sensitivity to flight velocity, whereas they are less affected by shaft angle variations. The influence of both velocity and shaft angle is non-uniformly dependent on frequency. Further, these figures demonstrate the high level of accuracy of the interpolation process proposed. In order to appreciate the sensitivity of identified model coefficients on flight parameters variation, figure 5.2 shows the location on the complex plane of the aeroelastic poles (eigenvalues of matrix A), for forward flight ranging from 0 kn to 80 kn (figure 5.2a), and shaft angle changing from -21° to 3° 5.2b. It is worth noting that, as expected, damping of poles is particularly affected by flight parameters variation, while their frequency remains almost unchanged.

Lastly, figure 5.3 shows the comparison between transfer function identified through the proposed ROM and those obtained with the complete, full-state, nonlinear model, for a flight condition not included in the database set. In particular, figure 5.3a depicts the transfer function between hub roll moment and lateral cyclic pitch control, for forward flight

5. Model stitching

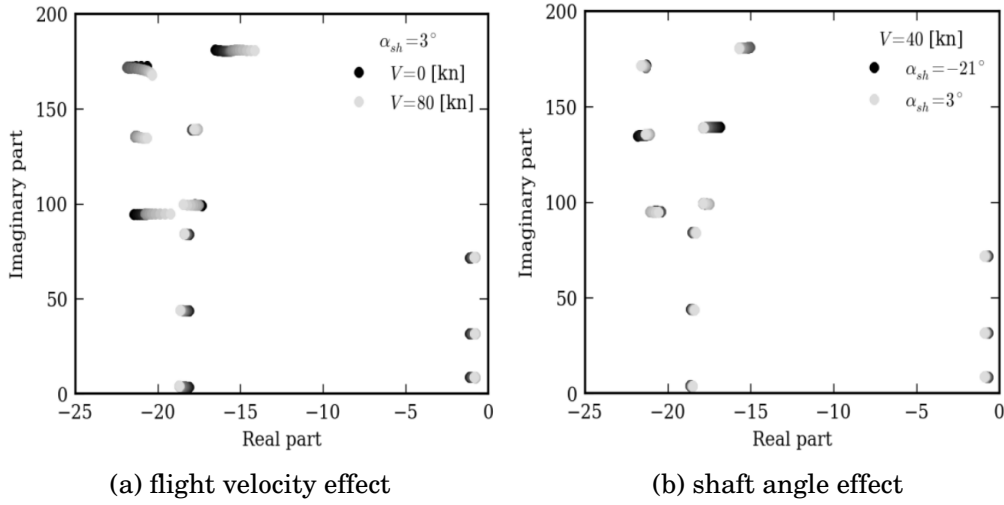


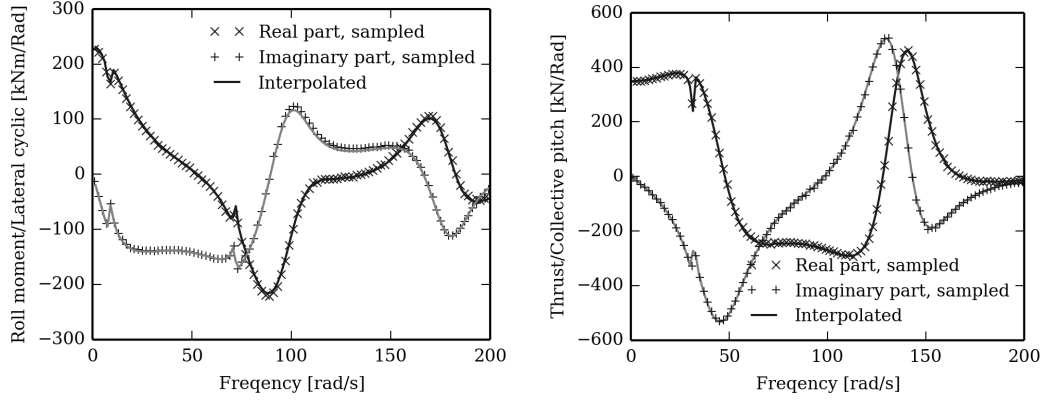
Figure 5.2.: Influence of flight parameters on poles of identified aeroelastic ROM.

velocity $V = 30\text{kn}$, whereas figure 5.3b presents the transfer function between thrust and collective pitch, for advancing velocity $V = 50\text{kn}$ (in both cases $\alpha_{sh} = 7.5^\circ$). The very good correlation shown in figure 5.3 between interpolated transfer functions and results directly given by the aeroelastic solver is a prove of the capability of the presented ROM to accurately estimate system aeroelastic response for arbitrary flight conditions inside the flight envelope of interest, which is an essential factor for the successful application of the proposed method in flight simulations.

5.2.2. Application to maneuvering flight

Below, the performance of the proposed main rotor model in predicting hub loads during maneuvering flights is assessed. First, it is applied to provide hub loads response to a periodic cyclic lateral pitch input with 1 rad/s frequency and 1-degree amplitude for a steady rectilinear, uniform, level flight condition with $V = 40\text{kn}$. In figure 5.4 the stitched model predictions (ROM) are compared with those given by the nonlinear, time-marching solution (NLTM) provided by the rotor aeroelastic tool also used to identify the model. Hub forces and moments from ROM simulation appear to be in good agreement with those determined by

5. Model stitching



(a) roll moment vs lat cyclic pitch, $V=30\text{kn}$ (b) thrust vs collective pitch, $V=50\text{kn}$

Figure 5.3.: Comparison between interpolated and sampled transfer functions for flight conditions not included in the database.

NLTM analysis.

Then, the state-space, ROM is applied to evaluate hub forces and moments generated by main rotor during a more complex unsteady Bo-105 maneuver. Starting from a steady level flight condition, the helicopter model follows a descent trajectory, initially at constant velocity and then operating a decelerated flight. Figure 5.5 depicts time histories of advance ratio μ , and shaft angle, α_{sh} . Corresponding hub motion and blade pitch controls, previously determined through a flight dynamics solver with lower-order rotor aeroelastic modeling, are used as input in this validation analysis. The capability of the proposed state-space ROM to accurately predict hub loads arising in unsteady helicopter maneuvering is assessed by comparison with loads given by NLTM solution. The corresponding results are presented in figure 5.6, which shows an very good correlation of time histories of hub force and moment components. These results demonstrate that the proposed model is able to yield aeroelastic responses in good agreement with those provided by complex, full-state, nonlinear aeroelastic tools.

5. Model stitching

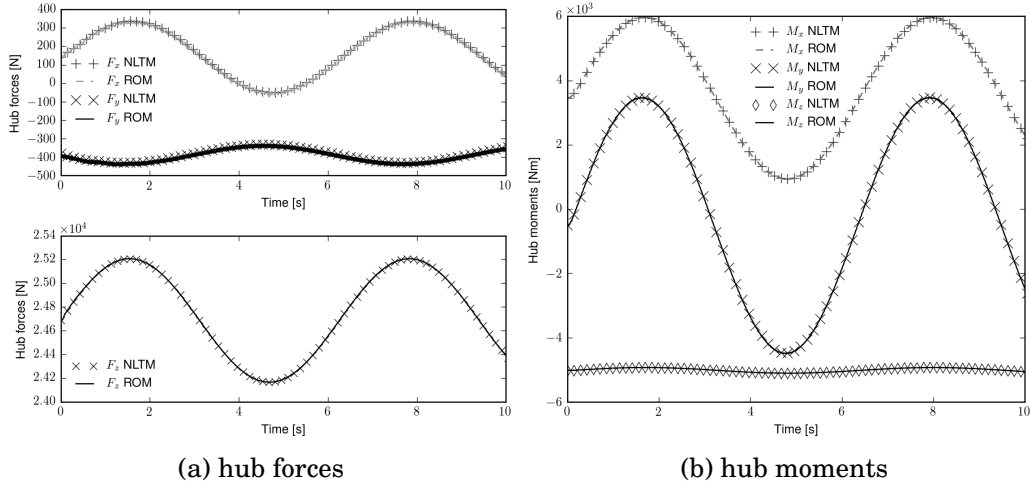


Figure 5.4.: Response to periodic lateral cyclic pitch. ROM vs NLTM.

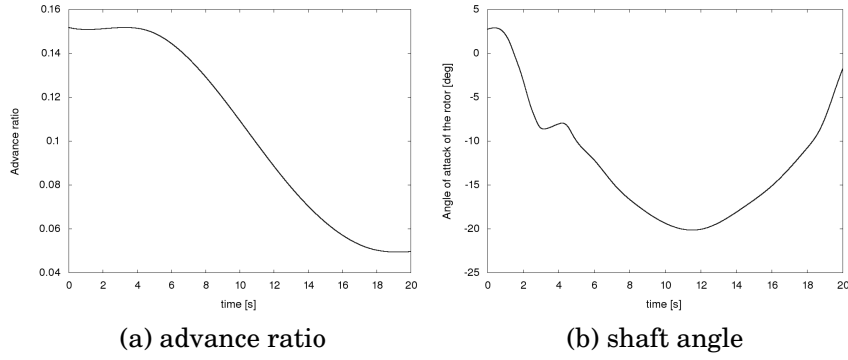


Figure 5.5.: Time histories of flight parameters during maneuver

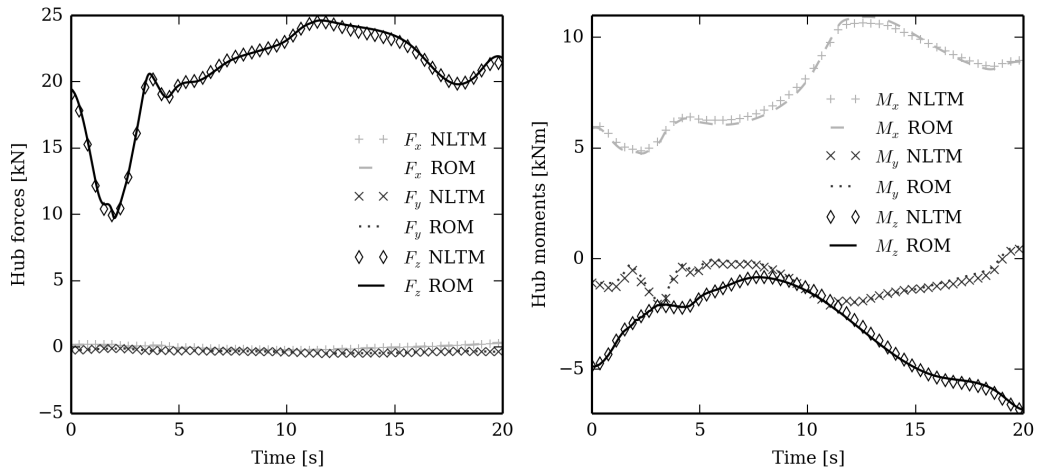


Figure 5.6.: Time histories of hub loads during maneuver flight. ROM vs NLTM.

6. Simulation results

The complete flight envelope model developed in this work was applied for the description of the aeroelastic behavior of the Bo105 helicopter main rotor. The Bo-105 is a light, twin-engine, multi-purpose helicopter developed by Bölkow of West Germany. It pioneered the rigid/hingeless rotorhead when it was introduced into service in 1970. Unless otherwise stated, the blades are modelled including one lag, two flapping and one torsional mode, and a complex wake inflow model derived by a free-wake potential-flow solver [BSCG13] is employed. This model is included and operated in SIMONA (SImulation, MOtion and NAvigation) Research Simulator (SRS), which is a six-degree-of-freedom simulator located at the Delft University of Technology (TU Delft), specifically designed for human-machine interaction and handling qualities research projects [SVPM03]. Among the available models included in SIMONA, a simple helicopter fuselage flight dynamics model is selected to be coupled with the introduced state-space main rotor model. It considers a tail rotor model based on the blade element theory with a quasi-dynamic inflow, a rigid-body model for the fuselage and includes the aerodynamic forces produced by fuselage and empennages.

In order to assess the suitability and level of fidelity of the proposed helicopter modelling for real-time helicopter flight simulations, it has been tested by two experienced test pilots who performed a wide range of maneuvers in the SRS. Pilots' feedback and data obtained from the simulations carried out are presented and discussed below, along with the identification of limits and required improvements of the simulation approach examined.

6. Simulation results

maneuver description	Group
Longitudinal step input	Control step input
Lateral step input	
Collective step input	
Pedal step input	
Autorotation	High gain tasks
Full collective	
Acceleration, deceleration	
Steady level flight	Steady maneuvers
Steady climb and descent	
Steady level turn	
Evolution from 20°	Free evolution
Evolution from forward flight	
Evolution from steady turn	
Spiral mode check	Modes check
Fugoid mode check	
Hover board	High frequency tasks
Longitudinal frequency sweep	

Table 6.1.: Performed maneuvers

6.1. Simulations summary

This section presents the results of the piloting simulations performed in the SIMONA Research Simulator at the Technical University of Delft, as driven by the finite-state rotor load model described in section 5. The scope of the test activity was twofold: (i) to assess the feasibility of application of the proposed rotor model in a real-time simulation device, and (ii) to collect pilot's feedback on the general perceived quality of simulation and on any issue raising during the tests. Two experienced test pilots have been asked to perform several maneuvers on the SIMONA Research Simulator driven by a Bo-105 helicopter model obtained by coupling the finite-state main rotor model of section 5 with the helicopter model already implemented in the SIMONA simulator.

Given the exploratory nature of this work and the type of the investigated maneuvers, only the advancing ratio, μ , was used to update the flight condition, y . However, it is worth noting that the computational power of SIMONA is estimated capable of working with updating based on more than three parameters.

6. Simulation results

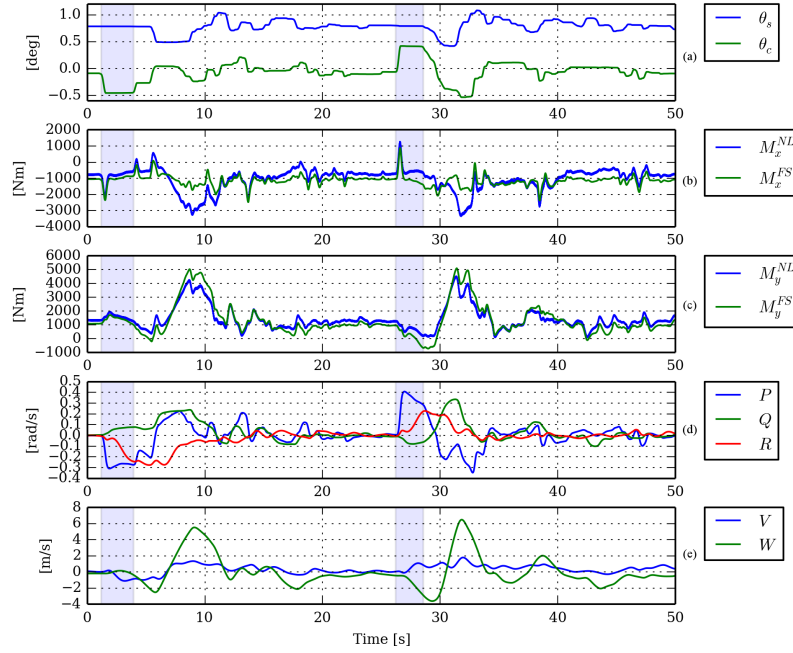


Figure 6.1.: Lateral step input at 50 kt.

All the simulations have been performed without any augmentation or control system. This choice is motivated by the intention of letting the pilot interact directly with the helicopter model, avoiding the implementation of tunable filters. For the same reason, the SIMONA motion system has been disabled. It is worth noting that neither of the pilots actually piloted a Bo-105 helicopter. The list of the maneuvers simulated is reported in Table 6.1.

In the overall, the pilots have asserted that the response to their commands of the simulator driven by the main rotor modeling presented in this work was realistic. However, they have provided specific comments for each maneuver flown.

In the following, the outcomes of some of those maneuvers for which pilots have observed an unusual or unexpected behavior of the simulator are discussed in detail. In particular, assuming helicopter kinematics and rotor blade controls as those of the considered maneuvers, the responses driven by the main rotor finite-state model (equal to the real-time ones provided by SIMONA) are compared with the responses evaluated off-line by the complete nonlinear rotor aeroelastic solver. The objective of the comparisons is to assess whether unusual or unexpected

6. Simulation results

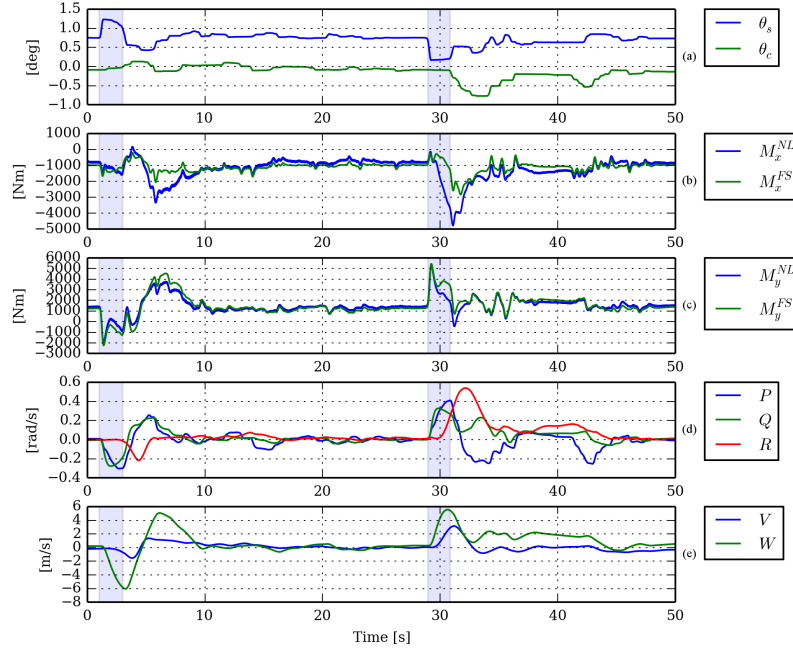


Figure 6.2.: Longitudinal cyclic step input at 50 kt.

simulator responses are due to the intrinsic characteristics of the complete nonlinear aeroelastic model applied or, rather, are produced by the approximations introduced by the finite state modeling.

6.1.1. Lateral step input

For the helicopter flying at velocity $U_0 = 50$ kt, the simulator response to a lateral cyclic, θ_c , step input is depicted in figure 6.1. As shown in figure 6.1(a), two θ_c step inputs are commanded by the pilot at the beginning of the observation period and after about 26 s. The pilot feedback on the simulated behavior has been positive, with a roll-pitch coupling of acceptable magnitude observed. In figure 6.1(d) the pitch-roll coupling is evidenced by the responses of the rolling, P , and pitching, Q , angular velocity components: the initial left blade cyclic pitch causes a left roll and a comparatively smaller nose up pitching, while a right blade cyclic pitch induces the opposite helicopter response. Soon after the initial cyclic step input, the helicopter starts turning and the pilot perceives a nose-down response: this is confirmed by the combination of the negative rolling with the significant negative yaw angular velocity, R . This

6. Simulation results

behavior has been deemed normal by both pilots.

Figures 6.1(b) and 6.1(c) depict the rolling and pitching moments as computed by the complete nonlinear solver (NL) and by the finite-state model used in the simulations (FS). The correlation between the two models is very good during the whole maneuver, except for two time intervals around 8 s and 30 s, where a considerable discrepancy between rolling moments is observed. This difference can be explained by the results in figure 6.1(e), where the values of the lateral velocity, V and the vertical velocity, W , are shown. Indeed, the load discrepancy is closely correlated with significant perturbations of velocity, W , which were not considered in the finite-state modelling adjournment (as mentioned earlier, the finite-state model is updated only as function of perturbations of the longitudinal helicopter velocity, U).

6.1.2. Longitudinal step input

Figure 6.2 shows the simulations resulting from two longitudinal step inputs, applied with the helicopter flying at velocity $U_0 = 50$ kt. In this case the pilot comments indicated a strong rolling acceleration following the control input. This is confirmed by the results in figure 6.2(d), where comparable variations of the angular velocities P and Q arise because of their remarkable coupling, after the step actuation of the longitudinal cyclic, θ_s . This coupling has been considered very strong by both pilots. Figures 6.2(b) and 6.2(c) prove that the rolling and pitching moments predicted by the two numerical models applied similar during the step inputs, and hence it may be concluded that such a behavior is directly related to the rotor aeroelastic model, rather than to the finite-state approximation. Akin to the lateral step input response, higher discrepancies between the predicted moments appear in combination with remarkable perturbations of vertical velocity W , as depicted in figure 6.2(e).

6. Simulation results

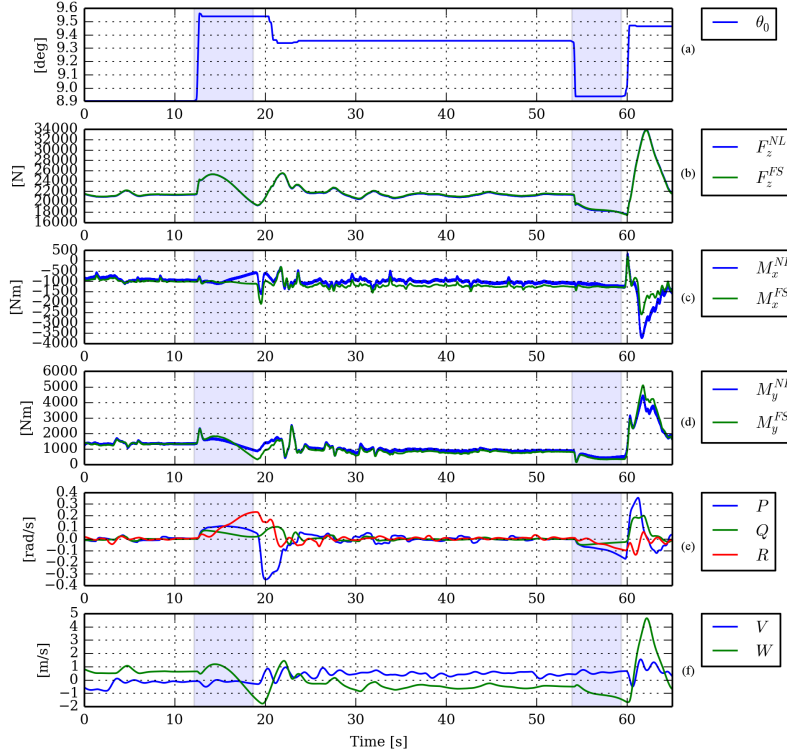


Figure 6.3.: Collective step input at 60 kt.

6.1.3. Collective step input

Next, flight simulation corresponding to a step input of the blade collective pitch is presented in figure 6.3. The pilot command has been actuated with the helicopter traveling at a constant velocity $U_0 = 60$ kt. Both pilots noted strong coupling with pitch and roll motions, as shown in figure 6.3(e). The first pilot has deemed the coupling of the collective blade pitch with the helicopter pitch significant but not necessarily unrealistic, while considered the corresponding roll coupling excessively strong. The second pilot noted a qualitative similarity of the overall cross coupling behavior experienced with that of the helicopter Agusta A109.

In figure 6.3(b) the rotor thrust predicted by the finite-state model is compared with that predicted by the nonlinear solver, while Figs. 6.3(c) and 6.3(d) show rolling and pitching moments given by the simulation approaches. The correlation between the two models is excellent, particularly for the vertical forces and the pitching moment. Small discrepancies appear between the rolling moment predictions. This proves that

6. Simulation results

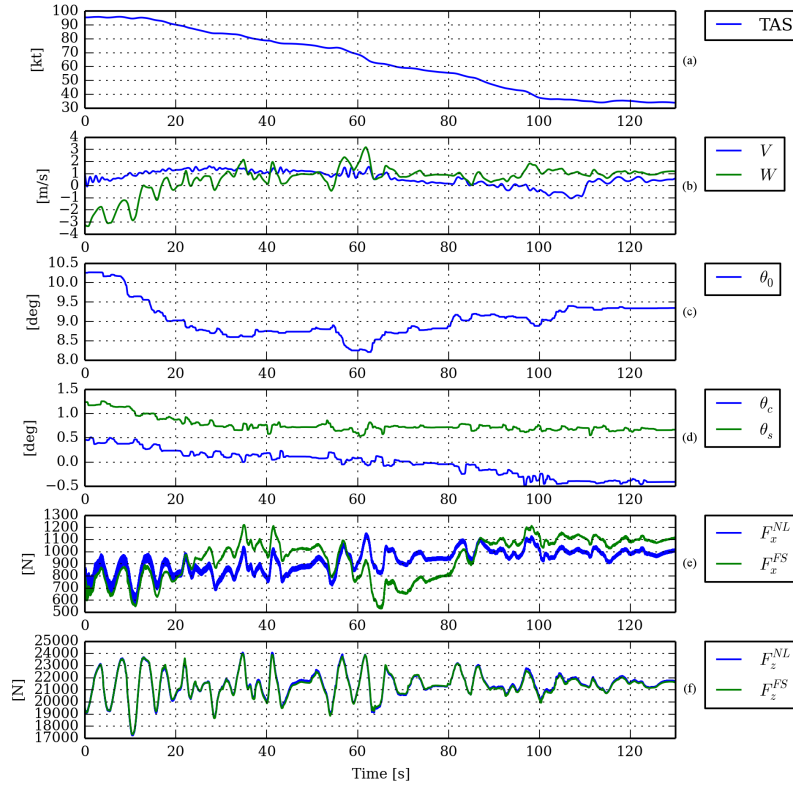


Figure 6.4.: Deceleration with blade flap, lag and torsional modes.

the cross coupling behavior observed derives directly from the nonlinear aeroelastic rotor model and is not due to approximations of the finite-state modeling.

6.1.4. Deceleration maneuver

In this section the deceleration maneuver performed by the second pilot using two different helicopter models is analyzed. The objective of this maneuver has been the comparison between simulations based on the model including flap, lag and torsional blade modes (see figure 6.4) and simulations based on the model including only the blade flap mode (see figure 6.5).

As shown in Figs. 6.4(a) and 6.5(a) the maneuver starts at $U_0 = 100$ kt and is composed of segments where the velocity decays of 20 kt followed by helicopter re-trimming.

The pilot did not notice significant differences between the responses

6. Simulation results

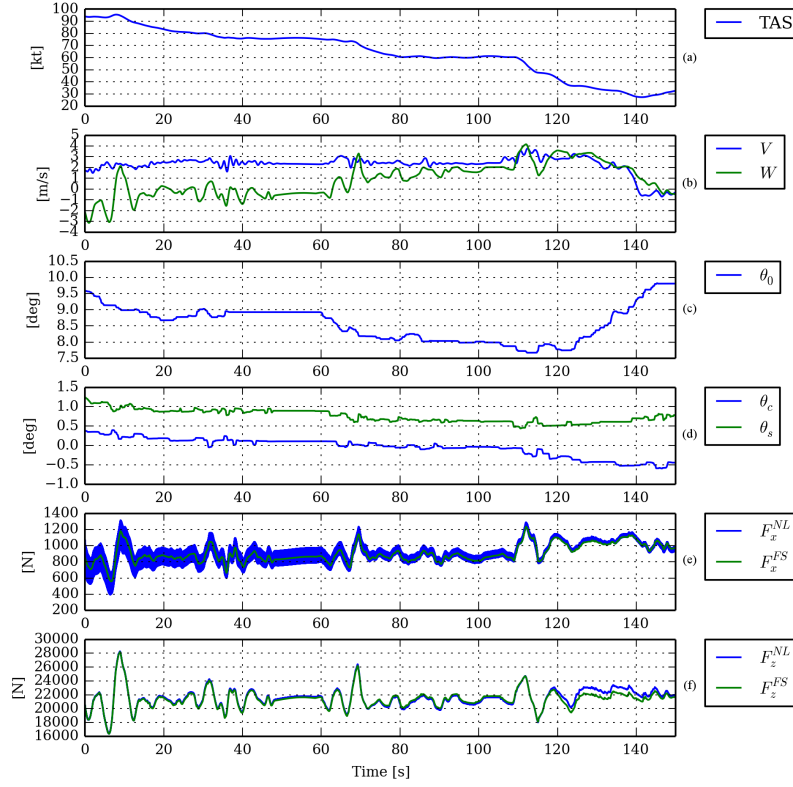


Figure 6.5.: Deceleration with one blade flapping mode.

from the two models, highlighting just a slightly decreased capability of the helicopter to maintain the trimmed speed around $U_0 = 100$ kt.

It is interesting to note that the rotor thrust predicted by both finite-state models (see Figs. 6.4(f) and 6.5(f)) is in good agreement with that computed by the corresponding nonlinear solver, while some differences appear between the x -axis forces determined by the three-mode model (see Figs. 6.4(e) and 6.5(e)). Indeed, figure 6.4(e) shows that the high frequency characteristics of the forces are predicted with good accuracy, but a relevant discrepancy is present on the low frequency load content during the whole maneuver.

For both blade models, 4/rev oscillations are present in the x -axis forces computed by the nonlinear solver, with a larger amplitude for the only-flap-mode case. These oscillations are not present in the finite-state model results, in that filtered out by the process of identification of the coefficients of the differential form describing the hub loads as functions of the hub motion [SCG14, GPPG14]. The spectral analysis reveals also

6. Simulation results

the presence of 80 rad/s oscillations in the three-mode case x -axis forces, corresponding to the frequency of the aeroelastic progressive lag mode.

6.2. Open loop simulations with an improved model

As mentioned in section 5.1, after the simulation tests were carried out, the full-flight envelope model was improved by removing a numerical cancellation issue caused by the additional states dynamics. This issue caused a less accurate prediction of the forces and moments when the contribution of the additional states dynamic was prevalent in the simulation. Even if the results obtained in the simulation tests, and presented above, remains valid, it is worth pointing out they are not completely indicative of the accuracy of the stitched model.

To show the accuracy obtainable with the improved model a lateral step input maneuver similar to that presented in 6.1.1 is shown in figure 6.6, while an acceleration maneuver is presented in figure 6.7. These maneuvers are simulated in open-loop by using the kinematics and control data obtained from the simulations. The forces computed by the reduced order model are compared with those predicted by the full order nonlinear aeroelastic solver in a similar fashion to the previous sections.

Comparing the results of figure 6.1.1 with those presented in figure 6.1 it is clear that the improved model leads to a better correlation of the results, especially in the description of the transient dynamics. The same is true for figure 6.7, in which also the periodic component of the vertical force is now well captured by the simulation model.

6. Simulation results

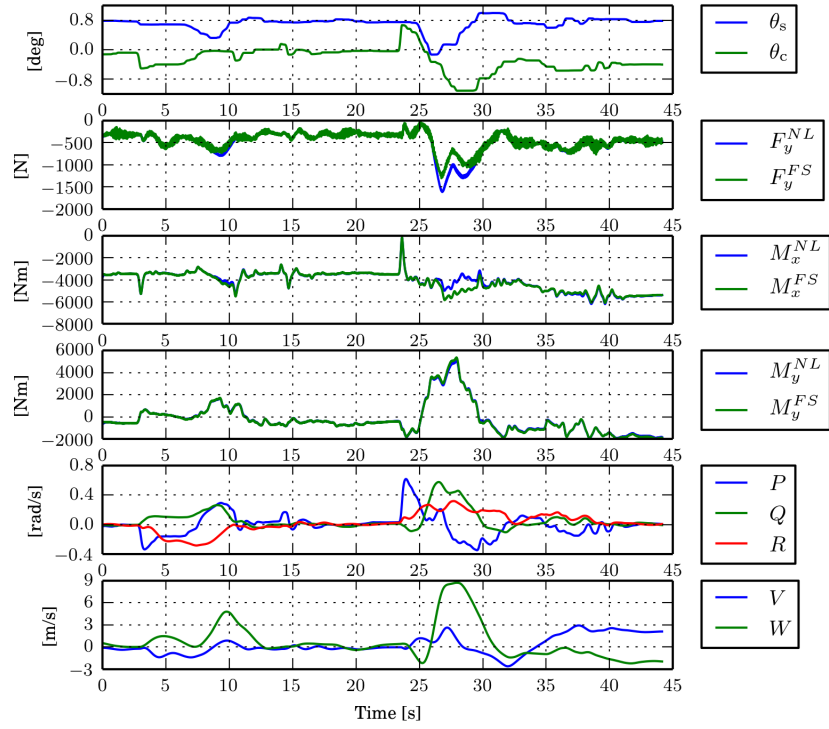


Figure 6.6.: Lateral step input at 60 kt

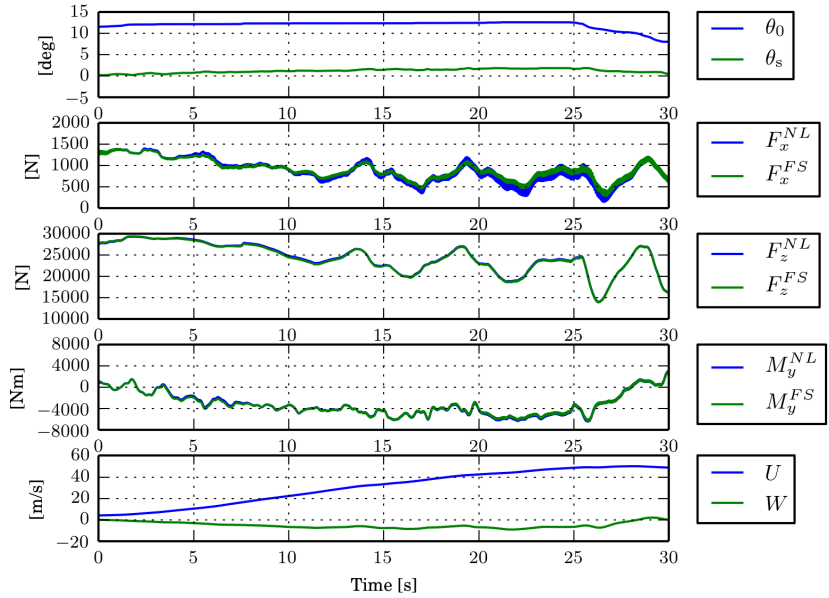


Figure 6.7.: Acceleration from 0 to 100 kt.

7. Concluding remarks

Development and accuracy assessment of a helicopter main rotor aeroelastic state-space models aimed at real-time maneuvering flight simulations have been presented. In particular three aeroelastic models concerning the aeroelastic behavior of helicopter rotors describing the hub loads generated by hub motion and pilot blade pitch controls have been presented:

1. a linear time invariant perturbation model, suitable for aeromechanic stability analyses and control systems developments;
2. a linear time periodic perturbation model, to be used when the linear time invariant approximation is not valid;
3. a full flight envelope model, developed specifically for flight simulation tasks.

These three models are extracted from arbitrary high-fidelity aeroelastic solvers through a methodology specifically developed in this work. In particular a novel model stitching technique was introduced for the definition of the full flight envelope model. It uses a suited optimization process that allows the identification of model matrices for any flight condition within the flight envelope of interest, starting from a pre-defined flight conditions database. The numerical investigation has demonstrated the capability of the modeling process presented to identify with an excellent level of accuracy main rotor aeroelastic transfer functions, in any operational condition within the flight envelope considered. Moreover, the application of the proposed state-space ROM for evaluating main rotor loads transmitted to the airframe during arbitrary unsteady maneuvers has provided results in good agreement with those predicted directly by the complex, full-state, nonlinear, time-marching aeroelastic solver.

7. Concluding remarks

This model has been then integrated inside the existing flight simulator SIMONA at the Delft University of Technology. The resulting complete helicopter model has been thoroughly tested by two experienced pilots, who performed several maneuvers with the aim of assessing its limitations and giving a feedback on the overall quality of the simulation. The data obtained from the simulations have been analyzed finding out that the models proposed is well suitable for real-time predictions to be used within flight simulators, and that is capable to reproduce accurately the aeroelastic forces generated by the rotor.

Bibliography

- [BL00a] Mahendra J Bhagwat and J Gordon Leishman. On the aerodynamic stability of helicopter rotor wakes. In *Proceedings of 56th annual forum of the American Helicopter Society, Virginia Beach, VA*, pages 2–4. Citeseer, 2000.
- [BL00b] Mahendra J Bhagwat and J Gordon Leishman. Time-accurate free-vortex wake model for dynamic rotor response. In *Proceedings of the Specialist Meeting of the American Helicopter Society*, 2000.
- [BL01] Mahendra J Bhagwat and J Gordon Leishman. Transient rotor inflow using a time-accurate free-vortex wake model. 2001.
- [BL03] Mahendra J Bhagwat and J Gordon Leishman. Rotor aerodynamics during maneuvering flight using a time-accurate free-vortex wake. *Journal of the American Helicopter Society*, 48(3):143–158, 2003.
- [BLP99] Ashish Bagai, J Gordon Leishman, and Jacob Park. Aerodynamic analysis of a helicopter in steady maneuvering flight using a free-vortex rotor wake model. *Journal of the American Helicopter Society*, 44(2):109–120, 1999.
- [BSCG13] G Bernardini, J Serafini, M Molica Colella, and M Gennaretti. Analysis of a structural-aerodynamic fully-coupled formulation for aeroelastic response of rotorcraft. *Aerospace Science and Technology*, 29(1):175–184, 2013.
- [CGB⁺15] Felice Cardito, Riccardo Gori, Giovanni Bernardini, Jacopo Serafini, and Massimo Gennaretti. Finite-state dynamic wake inflow modelling for coaxial rotors. In *Proceedings*

Bibliography

of the 41st European Rotorcraft Rorum 2015, Munich (Germany), Sept. 1-4. DGLR and TU Munchen, 2015.

- [Cla76] JMC Clark. The consistent selection of parameterizations in system identification. In *Joint Automatic Control Conference*, number 13, pages 576–580, 1976.
- [DPA⁺07] James Downs, Ron Prentice, S Alzell, Adam Besachio, CM Ivler, Mark B Tischler, and MH Mansur. Control system development and flight test experience with the mq-8b fire scout vertical take-off unmanned aerial vehicle (vtuav). In *Annual Forum Proceedings-American Helicopter Society*, volume 63, page 566. AMERICAN HELICOPTER SOCIETY, INC, 2007.
- [GB07] Massimo Gennaretti and Giovanni Bernardini. Novel boundary integral formulation for blade-vortex interaction aerodynamics of helicopter rotors. *AIAA journal*, 45(6):1169–1176, 2007.
- [GCM00] M Gennaretti, A Corbelli, and F Mastroddi. A comparison among some aeroelastic models for the stability analysis of a flap-lag-torsion helicopter rotor in hover. In *EUROPEAN ROTORCRAFT FORUM*, volume 26, pages 68–68. AAAF; 1998, 2000.
- [GCS⁺13] Massimo Gennaretti, MM Collela, Jacopo Serafini, B Dang Vu, P Masarati, Giuseppe Quaranta, Vincenzo Muscarello, Michael Jump, Michael Jones, Linghai Lu, et al. Anatomy, modelling and prediction of aeroservoelastic rotorcraft-pilot-coupling. In *39th European Rotorcraft Forum*, 2013.
- [GG82] M. Gennaretti and L. Greco. A time-dependent coefficient reduced-order model for unsteady aerodynamics of propellers. *Journal of Aircraft*, 42(1):138–147, 1982.
- [GG08] M Gennaretti and L Greco. Whirl flutter analysis of propellers using unsteady aerodynamics reduced-order models. *Aeronautical Journal*, 112(1131):233–242, 2008.
- [GGP⁺15] Riccardo Gori, Massimo Gennaretti, Marilena D Pavel, Olaf Stroosma, and Ivan Miletovic. Prediction and sim-

Bibliography

- ulator verification of state-space rotor modelling on helicopter manoeuvring flight. In *Proceedings of the 41st European Rotorcraft Rorum 2015, Munich (Germany), Sept. 1-4*. DGLR and TU Munchen, 2015.
- [GGS⁺15] M Gennaretti, R Gori, J Serafini, G Bernardini, and F Cardito. Rotor dynamic wake inflow finite-state modelling. In *33rd AIAA Applied Aerodynamics Conference, Dallas, TX*, 2015.
- [GGS⁺16] M Gennaretti, R Gori, J Serafini, G Bernardini, and F Cardito. A space-time accurate finite-state inflow model for aeroelastic applications. In *72nd Annual Forum and Technology Display, West Palm Beach, Florida USA, May 17-19*, 2016.
- [GM12] M. Gennaretti and D. Muro. Multiblade reduced-order aerodynamics for state-space aeroelastic modeling of rotors. *J. of Aircraft*, 49(2):495–502, 2012.
- [GP73] Gene H Golub and Victor Pereyra. The differentiation of pseudo-inverses and nonlinear least squares problems whose variables separate. *SIAM Journal on numerical analysis*, 10(2):413–432, 1973.
- [GPPG14] Riccardo Gori, Francesca Pausilli, Marilena D Pavel, and Massimo Gennaretti. State-space rotor aeroelastic modeling for real-time helicopter flight simulation. In *Advanced Materials Research*, volume 1016, pages 451–459. Trans Tech Publ, 2014.
- [GSMQ13] Massimo Gennaretti, Jacopo Serafini, Pierangelo Masarati, and Giuseppe Quaranta. Effects of biodynamic feedthrough in rotorcraft/pilot coupling: collective bounce case. *Journal of Guidance, Control, and Dynamics*, 36(6):1709–1721, 2013.
- [Gui75] Roberto Guidorzi. Canonical structures in the identification of multivariable systems. *Automatica*, 11(4):361–374, 1975.

Bibliography

- [GVL12] Gene H Golub and Charles F Van Loan. *Matrix computations*, volume 3. JHU Press, 2012.
- [HD74] Dewey H Hodges and EH Dowell. Nonlinear equations of motion for the elastic bending and torsion of twisted nonuniform rotor blades. 1974.
- [Hig02] Nicholas J Higham. *Accuracy and stability of numerical algorithms*. Siam, 2002.
- [HP93] Chengjian He and David A Peters. Finite state aeroelastic model for use in rotor design optimization. *Journal of aircraft*, 30(5):777–784, 1993.
- [HTD99] K Hall, J Thomas, and E Dowell. Reduced-order modeling of unsteady small-disturbance flows using a frequency-domain proper orthogonal decomposition technique. *identity*, 5(679):8, 1999.
- [Joh14] Steven G Johnson. The nlopt nonlinear-optimization package, 2014.
- [Kar82] Mordechay Karpel. Design for active flutter suppression and gust alleviation using state-space aeroelastic modeling. *Journal of Aircraft*, 19(3):221–227, 1982.
- [KNB04] Tanyoun Kim, Kanivenahalli S Nagaraja, and Kumar G Bhatia. Order reduction of state-space aeroelastic models using optimal modal analysis. *Journal of aircraft*, 41(6):1440–1448, 2004.
- [KPP99] Krishnamohan R Krothapalli, JVR Prasad, and David A Peters. Study of a rotor flap-inflow model including wake distortion terms. DTIC Document, 1999.
- [Lju98] Lennart Ljung. *System identification*. Springer, 1998.
- [LPL14] E Louarroudi, R Pintelon, and J Lataire. Accurate frequency domain measurement of the best linear time-invariant approximation of linear time-periodic systems including the quantification of the time-periodic distortions. *Mechanical Systems and Signal Processing*, 48(1):274–299, 2014.

Bibliography

- [Lue67] David G Luenberger. Canonical forms for linear multivariable systems. *Automatic Control, IEEE Transactions on*, 12(3):290–293, 1967.
- [MF05] Luigi Morino and Alessia Ferrante. A method for evaluating an aerodynamic-matrix reduced-order model. In *Atti del XVIII Congresso Nazionale AIDAA, Volterra, Italy, September 19-22, 2005*. AIDAA, 2005.
- [MH96] Tomas McKelvey and Anders Helmersson. State-space parametrizations of multivariable linear systems using tridiagonal matrix forms. In *Decision and Control, 1996., Proceedings of the 35th IEEE Conference on*, volume 4, pages 3654–3659. IEEE, 1996.
- [MMDT⁺95] L Morino, F Mastroddi, R De Troia, GL Ghiringhelli, and P Mantegazza. Matrix fraction approach for finite-state aerodynamic modeling. *AIAA journal*, 33(4):703–711, 1995.
- [MQM⁺15] Vincenzo Muscarello, Giuseppe Quaranta, Pierangelo Masarati, Linghai Lu, Michael Jones, and Michael Jump. Prediction and simulator verification of roll/lateral adverse aeroservoelastic rotorcraft–pilot couplings. *Journal of Guidance, Control, and Dynamics*, pages 1–19, 2015.
- [Pit80] Dale M Pitt. Rotor dynamic inflow derivatives and time constants from various inflow models. Technical report, DTIC Document, 1980.
- [PJDV⁺13] Marilena D Pavel, Michael Jump, Binh Dang-Vu, Pierangelo Masarati, Massimo Gennaretti, Achim Ionita, Larisa Zaichik, Hafid Smaili, Giuseppe Quaranta, Deniz Yilmaz, et al. Adverse rotorcraft pilot couplings - past, present and future challenges. *Progress in Aerospace Sciences*, 62:1–51, 2013.
- [PMD⁺11] MD Pavel, J Malecki, B DangVu, P Masarati, M Gennaretti, M Jump, M Jones, H Smaili, A Ionita, and L Zaicek. Present and future trends in rotorcraft pilot couplings (rpcs) - a retrospective survey of recent research

Bibliography

- activities within the european project aristotel. *Gallarate, Italy*, pages 13–14, 2011.
- [PP81] Dale M Pitt and David A Peters. Theoretical prediction of dynamic-inflow derivatives. *Vertica*, 5(1):21–34, 1981.
- [PT12] Les Piegl and Wayne Tiller. *The NURBS book*. Springer Science & Business Media, 2012.
- [PWP⁺13] MD Pavel, M White, GD Padfield, G Roth, M Hamers, and A Taghizad. Validation of mathematical models for helicopter flight simulators past, present and future challenges. *Aeronautical Journal*, 117(1190):343–388, 2013.
- [QKWB99] TR Quackenbush, JD Keller, DA Wachspress, and AH Boschitsch. Reduced order free wake modeling for near real time simulation of rotorcraft flight mechanics. In *ANNUAL FORUM PROCEEDINGS-AMERICAN HELICOPTER SOCIETY*, volume 55, pages 481–497, 1999.
- [QTM⁺14] Giuseppe Quaranta, Aykut Tamer, Vincenzo Muscarello, Pierangelo Masarati, Massimo Gennaretti, Jacopo Serafini, and Marco Molica Colella. Rotorcraft aeroelastic stability using robust analysis. *CEAS Aeronautical Journal*, 5(1):29–39, 2014.
- [RKH⁺15] O Rand, V Khromov, S Hersey, R Celi, O Juhasz, and M Tischler. Linear inflow model extraction from high-fidelity aerodynamic models for flight dynamics applications. In *Proceedings of the 71st Annual Forum of the American Helicopter Society, Virginia Beach, VA*, 2015.
- [SCG14] Jacopo Serafini, Marco Molica Colella, and Massimo Gennaretti. A finite-state aeroelastic model for rotorcraft–pilot coupling analysis. *CEAS Aeronautical Journal*, 5(1):1–11, 2014.
- [SCH05] Sang Joon Shin, Carlos ES Cesnik, and Steven R Hall. System identification technique for active helicopter rotors. *Journal of intelligent material systems and structures*, 16(11-12):1025–1038, 2005.

Bibliography

- [SGM⁺08] J Serafini, M Gennaretti, P Masarati, G Quaranta, O Dieterich, et al. Aeroelastic and biodynamic modeling for stability analysis of rotorcraft-pilot coupling phenomena. In *Proceedings of the 34th European Rotorcraft Forum*, 2008.
- [Sha70] David F Shanno. Conditioning of quasi-newton methods for function minimization. *Mathematics of computation*, 24(111):647–656, 1970.
- [Sid01] Afreen Siddiqi. *Identification of the harmonic transfer functions of a helicopter rotor*. PhD thesis, Massachusetts Institute of Technology, 2001.
- [SVPM03] Olaf Stroosma, MM Van Paassen, and Max Mulder. Using the simona research simulator for human-machine interaction research. In *AIAA modeling and simulation technologies conference*, 2003.
- [TC00] C Theodore and Roberto Celi. Flight dynamic simulation with refined aerodynamics and flexible blade modeling. In *ANNUAL FORUM PROCEEDINGS-AMERICAN HELICOPTER SOCIETY*, volume 56, pages 857–872. AMERICAN HELICOPTER SOCIETY, INC, 2000.
- [The49] Theodore Theodorsen. General theory of aerodynamic instability and the mechanism of flutter. 1949.
- [TR06] Mark B Tischler and Robert K Remple. Aircraft and rotorcraft system identification. *AIAA education series*, 2006.
- [TTBH15] Eric L Tobias, Mark B Tischler, Tom Berger, and Steven G Hagerott. Full flight-envelope simulation and piloted fidelity assessment of a business jet using a model stitching architecture. In *AIAA Modeling and Simulation Technologies Conference*, page 1594, 2015.
- [VV07] Michel Verhaegen and Vincent Verdult. *Filtering and system identification: a least squares approach*. Cambridge university press, 2007.
- [Wel67] Peter D Welch. The use of fast fourier transform for the estimation of power spectra: A method based on time averag-

Bibliography

- ing over short, modified periodograms. *IEEE Transactions on audio and electroacoustics*, 15(2):70–73, 1967.
- [WH90] Norman M Wereley and Steven R Hall. Frequency response of linear time periodic systems. In *Decision and Control, 1990., Proceedings of the 29th IEEE Conference on*, pages 3650–3655. IEEE, 1990.
- [ZPP04] Jinggen Zhao, JVR Prasad, and David A Peters. Rotor dynamic wake distortion model for helicopter maneuvering flight. *Journal of the American Helicopter Society*, 49(4):414–424, 2004.
- [ZT10] Lior Zivan and Mark B Tischler. Development of a full flight envelope helicopter simulation using system identification. *Journal of the American Helicopter Society*, 55(2):22003–22003, 2010.

A. Understanding the meaning of the RMA poles

In order to show the meaning of poles of the state-space aeroelastic models presented, let us consider the linearized, multiblade-variable, constant-coefficient aeroelastic model of an isolated helicopter rotor.

For \mathbf{u} denoting the vector of hub motion variables and blade controls (see 2.2.1), and \mathbf{z} denoting the vector of rotor blade dynamics state-space variables, in frequency domain, hub loads resulting by the sum of aerodynamic and inertial forces acting on the blades can be formally expressed as:

$$\tilde{\mathbf{f}}_{MR} = (\mathbf{f}_0 + s\mathbf{f}_1) \tilde{\mathbf{z}} + (\mathbf{G}_0 + s\mathbf{G}_1 + s^2\mathbf{G}_2) \tilde{\mathbf{u}} \quad (\text{A.1})$$

where:

$$\mathbf{z} = \begin{Bmatrix} \mathbf{q}_b \\ \dot{\mathbf{q}}_b \\ \mathbf{r}_{aero} \end{Bmatrix} \quad (\text{A.2})$$

with \mathbf{q}_b and \mathbf{r}_{aero} denoting, respectively, vector of (rigid and/or elastic) blade degrees of freedom and vector of additional aerodynamic states (present when unsteady aerodynamics modeling is applied [GM12, GCM00, GG82]).

On the other hand, rotor blade dynamics is governed by a set of differential equations in state-space form of the following type:

$$s\tilde{\mathbf{z}} = \mathbf{D}\tilde{\mathbf{z}} + (\mathbf{E}_0 + s\mathbf{E}_1 + s^2\mathbf{E}_2) \tilde{\mathbf{x}} \quad (\text{A.3})$$

where \mathbf{D} is the rotor aeroelastic state matrix. The external forcing terms would disappear in fixed-hub, fixed-control analysis.

Thus, solving A.1 for $\tilde{\mathbf{z}}$ and substituting in A.3, the following expression

A. Understanding the meaning of the RMA poles

for the hub loads is obtained:

$$\begin{aligned}\tilde{\mathbf{f}}_{MR} &= [(\mathbf{f}_0 + s\mathbf{f}_1)(s\mathbf{I} - \mathbf{D})^{-1}(\mathbf{E}_0 + s\mathbf{E}_1 + s^2\mathbf{E}_2) + (\mathbf{G}_0 + s\mathbf{G}_1 + s^2\mathbf{G}_2)] \tilde{\mathbf{x}} \\ &= \mathbf{H}_a(s) \tilde{\mathbf{x}}\end{aligned}\tag{A.4}$$

It yields the straightforward identification of the analytical transfer matrix, \mathbf{H}_a , relating hub loads to hub motion and blade controls.

The application to matrix $\mathbf{H}_a(s)$ of the RMA considered in this work provides the matrix \mathbf{A} of the state-space model coinciding with the rotor aeroelastic state matrix, \mathbf{D} (namely, the poles of the RMA coincide with the rotor aeroelastic eigenvalues). This is demonstrated by considering the following Woodbury matrix identity [Hig02]

$$(\mathbf{z} + \mathbf{U} \mathbf{W} \mathbf{V})^{-1} = \mathbf{z}^{-1} - \mathbf{z}^{-1} \mathbf{U} (\mathbf{W}^{-1} + \mathbf{V} \mathbf{z}^{-1} \mathbf{U})^{-1} \mathbf{V} \mathbf{z}^{-1} \tag{A.5}$$

where \mathbf{W} and \mathbf{z} are invertible square matrices and \mathbf{U} and \mathbf{V} denote matrices of appropriate dimensions. Indeed, for $\mathbf{z} = s\mathbf{I}$ and $\mathbf{W} = \mathbf{I}$, the pre-multiplication with $s\mathbf{N}$, the post-multiplication with \mathbf{M} , followed by the assumptions $\mathbf{U} = \mathbf{I}$, $\mathbf{V} = -\mathbf{K}$, or $\mathbf{U} = -\mathbf{K}$, $\mathbf{V} = \mathbf{I}$, yield the identities

$$s\mathbf{N}(s\mathbf{I} - \mathbf{K})^{-1}\mathbf{M} = \mathbf{N}\mathbf{M} + \mathbf{N}(s\mathbf{I} - \mathbf{K})^{-1}\mathbf{K}\mathbf{M} = \mathbf{N}\mathbf{M} + \mathbf{N}\mathbf{K}(s\mathbf{I} - \mathbf{K})^{-1}\mathbf{M} \tag{A.6}$$

that are applied to determine the matrices of the RMA of the matrix \mathbf{H}_a in A.4, thus providing

$$\begin{aligned}\mathbf{D}_2 &= \mathbf{G}_2 + \mathbf{f}_1\mathbf{E}_2 \\ \mathbf{D}_1 &= \mathbf{G}_1 + \mathbf{f}_0\mathbf{E}_2 + \mathbf{f}_1\mathbf{E}_1 + \mathbf{f}_1\mathbf{D}\mathbf{E}_2 \\ \mathbf{D}_0 &= \mathbf{G}_0 + \mathbf{f}_0\mathbf{E}_1 + \mathbf{f}_0\mathbf{D}\mathbf{E}_2 + \mathbf{f}_1\mathbf{E}_0 + \mathbf{f}_1\mathbf{D}\mathbf{E}_1 + \mathbf{f}_1\mathbf{D}_2\mathbf{E}_2 \\ \mathbf{A} &= \mathbf{D} \\ \mathbf{B} &= \mathbf{E}_0 + \mathbf{D}\mathbf{E}_1 + \mathbf{D}^2\mathbf{E}_2 \\ \mathbf{C} &= \mathbf{f}_0 + \mathbf{f}_1\mathbf{D}\end{aligned}\tag{A.7}$$

The conclusion is that, for an arbitrary high-fidelity solver based on an unsteady aerodynamic formulation, the additional states introduced by the RMA represent rotor blade dynamics, as well as the aerodynamics

A. Understanding the meaning of the RMA poles

flow-memory effects due to unsteady wake vorticity and flow compressibility (if present).